https://doi.org/10.5194/egusphere-2025-1670
Preprint. Discussion started: 30 April 2025

Interannual variability of the Asian summer monsoon anticyclone

Oleh Kachula[1], Bärbel Vogel[1], Gebhard Günther[1], and Rolf Müller[1]

[1]Institute of Climate and Energy Systems (ICE-4), Forschungszentrum Jülich, Jülich, Germany

Correspondence: Oleh Kachula (o.kachula@fz-juelich.de)

Abstract.

The definition of the boundary of the Asian summer monsoon anticyclone (ASMA) in the upper troposphere and lower stratosphere (UTLS) (350-410 K) is a known challenge that highly impacts the information about the anticyclone's behavior and affects the results when studying of its interannual variability. We present a novel method based on the absolute vortex moments that defines the ASMA boundaries by solving an optimization problem. A 44-year ASMA climatology (1980-2023) will be shown using the ERA5 reanalysis provided by ECMWF. Here, we address the ASMA's climatology (1980-2023), interannual variability, the variability of the start and end dates and the duration of the anticyclone peak phase calculated with help of the defined novel method. In addition, three individual years – 2017, 2022 and 2023 are highlighted during which aircraft campaigns took place to measure air inside the ASMA or its outflow (StratoClim, ACCLIP, PHILEAS). The interannual analysis is based on the anticyclone's centroid latitude and longitude, excess kurtosis, angle, aspect ratio using 4 isentropic surfaces: 350, 370, 390 and 410 K. Our findings show that the ASMA area decreases over the period 1980-2023 in contrast to previous studies. Further, we provide evidence of possible bimodality of the ASMA by showing clustering of values (the Montgomery streamfunction values minus an optimized background value) around two centers on climatological data over 44 years as well as counting the number of days when two anticyclones (or two modes) where found simultaneously.

1 Introduction

The Asian summer monsoon anticyclone (ASMA) is an important upper troposphere-lower stratosphere (UTLS) meteorological circulation pattern in the Northern Hemisphere during boreal summer. The anticyclone spans from East Africa to the western Pacific connected with strong convection occurring over South and East Asia (Randel and Park 2006; Park et al. 2008). The Asian monsoon system plays a major role in uplifting near-surface emissions e.g., anthropogenic pollutants or greenhouse gases to the UTLS.

Within the ASMA trace gases as well as aerosols particles and their gas-phase precursors are confined and can be exported to the northern extra-tropical UTLS as well as to the global stratosphere. (e.g., Vogel et al. 2016; Ploeger et al. 2017; Yu et al. 2017; Adcock et al. 2021; Lauther et al. 2022; Yan et al. 2019; Ungermann et al. 2016)

https://doi.org/10.5194/egusphere-2025-1670
Preprint. Discussion started: 30 April 2025

Characterizing the inter-annual (and intra-seasonal) variability of the ASMA in terms of area, position, bimodality, shape and duration is important to understand if there are any trends or changes in the ASMA caused by climate change during the last decades (e.g., Lal et al. 2001; Kripalani et al. 2007; Turner and Annamalai 2012; Fadnavis et al. 2019; Basha et al. 2020).

Possible reasons for the variability of the Asian summer monsoon anticyclone are currently being discussed and include multiple large-scale climate phenomena, such as El Niño-Southern Oscillation (ENSO), Quasi-biennial oscillation (QBO), Indian Ocean Dipole (IOD). ENSO in particular, a key driver of global climate variability, affects the ASMA strength (in terms of the residual Montgomery streamfunction values) and position (Basha et al. 2020; Kumar and Ratnam 2021).

Manney et al. (2021) show that in the last decades (1979-2018) the ASMA underwent noticeable interannual change: its area is growing, the anticyclone is shifted to the north, its formation starts earlier and the brake-up phase ends later.

To be able to study the dynamical properties of the Asian summer monsoon anticyclone it is necessary to formally define it (Manney et al. 2021). Here, similar to Manney et al. (2021), we characterize the ASMA by considering the Montgomery streamfunction (or potential) μ on an isentropic surface, which is defined as

$$\mu = c_p T + \Phi \tag{1}$$

where, c_p is the specific heat capacity at constant pressure, T is temperature and $\Phi = gz$ is the geopotential, with gravitational acceleration g and height z.

There is a debate how to define the edge of the anticyclone best (e.g., Ploeger et al. 2015) and the way defining it influences the boundary of maximum confinement of the ASMA (i.e., the edge of the anticyclone). A methodology to define the boundary impacts further analysis (Santee et al. 2017) and the conclusions that could be drawn on its interannual variability. Different ways to define the boundary of the ASMA exist. Previously the methodologies to define the ASMA were based on using several quantities, such as potential vorticity (Ploeger et al. 2015), although it provides only an enclosed contour in a very narrow range of potential temperatures, using gradient or anomalies fields of geopotential height (e.g. Zarrin et al. 2010; Barret et al. 2016; Nützel et al. 2016), and Montgomery streamfunction on isentropic surface (e.g. Popovic and Plumb 2001; Santee et al. 2017; Manney et al. 2021).

An additional difficulty for the definition of the edges of the ASMA is a “leaky” transport barrier which allows outflow out of the ASMA during the monsoon season (Dethof et al. 1999; Popovic and Plumb 2001; Garny and Randel 2013; Ploeger et al. 2013; Vogel et al. 2016). Further, the ASMA can potentially turn into a bimodal state (Zhang et al. 2002) introducing challenges to define the boundary.

Santee et al. (2017) defined the boundaries as an approximation of Montgomery streamfunction (MSF) values at the position where the strong wind speed gradients appear. After calculating MSF background values, Manney et al. (2021) applied moments analysis to calculate the centroid latitude and longitude, aspect ratio and excess kurtosis.

Santee et al. (2017) and Manney et al. (2021) use a single MSF background value per isentropic surface to determine the ASMA boundaries over one monsoon period (both individual months and JJA). The main challenge is to describe the ASMA during development and break-up phases, where MSF background values might be too small or too large to not enclose the

https://doi.org/10.5194/egusphere-2025-1670
Preprint. Discussion started: 30 April 2025

boundaries at all. To handle these special cases. Manney et al. (2021) filters out data when the ASMA area is less than 1% of the hemisphere area.

We propose a method to identify MSF background values for an individual point in time per isentropic surface in contrast to choosing one single value for one monsoon period. Thus in the approach presented here, an optimized MSF value to describe the ASMA boundaries will be presented reflecting the day-to-day variability of the ASMA. Our dynamical approach avoids some subjectivity of selecting the most suitable MSF value to enclose the ASMA boundaries. Another advantage of the proposed method is that it can be used on any time scale, choosing individual days or specific hours.

After retrieving a set of optimized MSF background values that are used to enclose the ASMA boundaries, we apply a moments analysis similar to Manney et al. (2021). To be able to compare our results to those by Manney et al. (2021), we show climatological values from 1980 to 2023, but instead of taking a fixed length period within each year (such as JJA), we define the peak phase of the ASMA.

In 2017, 2022 and 2023 aircraft measurement campaigns: StratoClim, ACCLIP and PHILEAS respectively were conducted in the region of the AMA, therefore in addition to the climatology we provide the moments analysis for the years 2017, 2022 and 2023 separately to compare these selected years with the 44-years climatology.

Part of StratoClim was an aircraft measurements campaign conducted on the Indian subcontinent over the southern side of the Himalayas between 30 July and 12 August (e.g., Singer et al. 2022, Vogel et al. 2023, Stroh and StratoClim-Team 2025). During StratoClim a variety of trace gases and aerosol characteristics were measured for the first time up to 20 km altitude in the ASMA to characterize major processes which dominate particle and trace gas transport from surface sources into the lower stratosphere.

The Asian Summer Monsoon Chemical and Climate Impacts Project (ACCLIP) was a comprehensive airborne field campaign operated during the monsoon season in August 2022. The campaign operated two research aircraft and ground-based balloon sounding equipped with instruments to measure trace gases and aerosol content over the Western Pacific region. The scientific objectives of ACCLIP campaign were to investigate how the anticyclone affects transport pathways of uplifted air to the UTLS. The measurements provide the insights into the chemical content composition, ozone chemistry, aerosol radiative effects and the role of distribution of Asian pollutants (Pan et al. 2024).

PHILEAS airborne campaign was conducted between August and October 2023 using the German research aircraft HALO (Riese et al. 2025). The campaign collected data that give insight into how the Asian summer monsoon anticyclone transport pollutants into the Northern extra-tropics. The campaign was split into two phases over different regions: in early to mid-August during the first measurement phase, monsoon air containing pollutants over the Eastern Mediterranean, Israel and Jordan were investigated; in the second phase, during flights from Anchorage, Alaska, the transport of polluted air over the Pacific, Alaska, and Canada was probed. The measurements provide an opportunity to study the polluted monsoon air at higher latitudes and altitudes up to the extratropical lower stratosphere, gathering the data on e.g., water vapor, methane, ozone concentration as well as aerosol and its gas-phase precursors.

In section 2, we explain the methodology to determine the boundaries of the ASMA, describe the peak phase of the ASMA and underscore challenges of the method, its advantages and disadvantages. Also we show the comparison of the calculated

https://doi.org/10.5194/egusphere-2025-1670
Preprint. Discussion started: 30 April 2025

MSF values with own novel method to Santee et al. (2017). Section 3 presents the horizontal distribution of the MSF residuals, climatological and individual time-series of the moments analysis, inter-annual variability of the ASMA area, centroid latitude and longitude.

2 Data description and methodology

2.1 The ERA5 dataset

For our study we use the ERA5 reanalysis (Hersbach et al. 2020) from the European Centre of Medium-Range Weather Forecasts (ECMWF) to calculate the Montgomery streamfunction. The range for interannual analysis covers the period 1980 to 2023, spanning April-October months within each year. We use a version of ERA5 with a resolution of 1×1, referred to as ERA5 $1^\circ \times 1^\circ$ (similar to Ploeger et al. 2021; Konopka et al. 2022; Clemens et al. 2024; Vogel et al. 2024). ERA5 $1^\circ \times 1^\circ$ data are directly provided by the ECMWF on a $1^\circ \times 1^\circ$ horizontal grid after down-scaling the original data provided on a $0.3^\circ \times 0.3^\circ$ horizontal grid. The vertical resolution (137 vertical levels up to 0.01 hPa) is not changed and is the same as in the original ERA5 reanalysis. For our analysis we use daily ECMWF data at noon (12:00 UTC).

2.2 Methodology

The analysis of the interannual variability of the Asian summer monsoon anticyclone depends on the choice of enclosing boundaries of the ASMA i.e., the location of the transport barrier of the ASMA. The problem is to define a contour line describing the boundary of the ASMA that coincidences with strong gradients of trace gases and aerosols found in measurements. The method proposed here to define the boundaries of the ASMA is based on the absolute vortex moment method that was already used to define the polar vortex (Matthewman et al., 2009).

The absolute vortex moment M_{kl} is given by

$$M_{kl}(\hat{\mu}, \mu_b) = \sum_{i=0}^{n-1} \sum_{j=0}^{m-1} (\hat{\mu}_{i,j} - \mu_b) y_i^k x_j^l \Delta y \Delta x \,, \tag{2}$$

with

$$\hat{\mu}_{i,j} := \begin{cases} \mu_{i,j} & \text{where } \mu_{i,j} \geq \mu_b \\ \mu_b & \text{where } \mu_{i,j} < \mu_b \end{cases} , \tag{3}$$

where $\mu_{i,j}$ is the Montgomery streamfunction defined on a regular grid of the size $n \times m$, for $i = 0, \ldots, n-1$, $j = 0, \ldots, m-1$; μ_b is a background value of MSF, y_i and x_j are latitude and longitude coordinates respectively, Δy and Δx are stepsizes over latitude and longitude axes respectively; k and l are non-negative integers that can be 0, 1 or 2 depending on what we want to

https://doi.org/10.5194/egusphere-2025-1670
Preprint. Discussion started: 30 April 2025

calculate. Because we use ERA5 reanalysis with $1^\circ \times 1^\circ$ grid resolution $\Delta x = 1$, $\Delta y = 1$, $n = 181$, $m = 360$, with

$$x_j := \begin{cases} j, & \text{if } 0 \leq j \leq 180 \\ 180 - j, & \text{if } 181 \leq j \leq 359 \end{cases}$$

and

$$y_i := 90 - i, \quad \text{if} \quad 0 \leq i \leq 180.$$

The method proposed by Matthewman et al. (2009) allows the aspect ratio (the ratio between the longitudinal and latitudinal axes of the equivalent ellipse), the angle between the equatorial axis and the major axis of the ellipse, the excess kurtosis and the coordinates of the center of the ASMA (ellipsoid center coordinates) to be retrieved (see Appendix A). The excess kurtosis (EK) serves as a measure of how far the shape is from the ellipse and can be used to investigate the bipolarity of the MSF distribution, ASMA splitting behavior into two anticyclones or strong eddy shedding events.

The anticyclone area is calculated separately because it is not based on the moments definitions. The information about the method is given below.

To calculate the moments quantities the method requires the so called background value of the parameter of choice (e.g., μ_b). Matthewman et al. (2009) use the mean poleward 45°N value of potential vorticity as the background value to encircle the polar vortex.

In case of the ASMA it is not possible to choose a specific region that should be averaged to obtain the background value, because several large scale monsoon systems (e.g., over America and Africa) exist in addition to the ASMA in contrast to the case of the polar vortex. Averaging different regions and hence varying the background value leads to change of the boundaries of the ASMA. Further, the ASMA is very variable in its shape and sometimes bimodal (Tibetan and Iranian mode) or trimodal (e.g. eddy shedding events) distributions occur (Zhang et al. 2002; Vogel et al. 2015; Nützel et al. 2016; Wang et al. 2022, Pan et al. 2024). This might cause issues with capturing the anticyclone and preserve unwanted noise.

The novelty compared to Manney et al. (2021) of the method proposed here consists of defining the region (ASMA box) that divides a global map in two parts and then introducing an objective function as ratio of absolute vortex moment calculated inside of two divided parts. Doing this we reformulate the task of enclosing the ASMA boundaries as an optimization problem where we can investigate the objective function to determine an optimized background value $\widetilde{\mu_b}$.

The ASMA box is defined based on our empirical knowledge that the anticyclone can be found in $[0^\circ N\text{-}90^\circ N, 0^\circ E\text{-}180^\circ E]$ region and serves to separate the Asian monsoon from other monsoon systems occurring during boreal summer such as the American or African monsoon.

By introducing the ASMA box it allows us to calculate M_{00}^{in} and M_{00}^{out} using Eq. (2) ($k = 0, l = 0$). The idea is that the values of Montgomery streamfunction inside of the dominant anticyclone region are higher than majority of $\hat{\mu}_{i,j}$ values outside of the ASMA box, so we can find such μ_b that keeps M_{00}^{out} minimal while maximize M_{00}^{in}. Using this idea we introduce the objective function as ratio of absolute vortex moments inside and outside of the ASMA box. The objective function

https://doi.org/10.5194/egusphere-2025-1670
Preprint. Discussion started: 30 April 2025

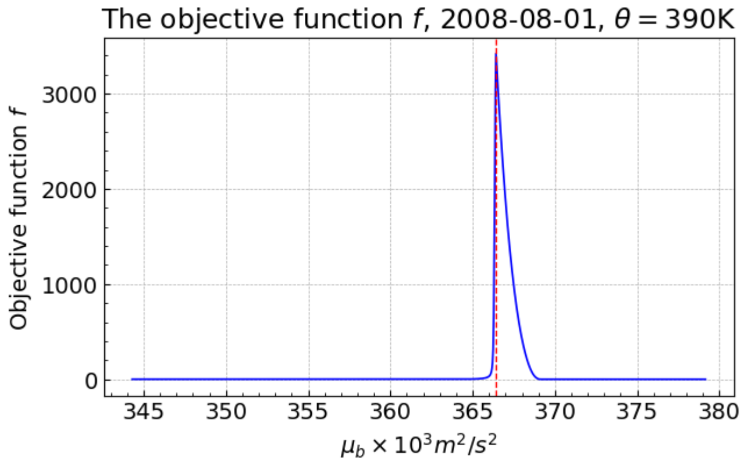

Figure 1. The objective function $f(\mu_b \mid \hat{\mu})$ depending on the background value μ_b for 1st August 2008 at 390 K. The maximum around $\widetilde{\mu_b} \approx 366.4$ is the optimized background value. There MSF values inside of the box are larger than outside.

$$f(\mu_b \mid \hat{\mu}_{i,j}) = \frac{M_{00}^{\text{in}}(\hat{\mu}_{i,j}, \mu_b)}{M_{00}^{\text{out}}(\hat{\mu}_{i,j}, \mu_b) + 1}, \tag{4}$$

should be maximized to determine the optimized boundary. By adding "+1" $(\mathrm{m}^2/\mathrm{s}^2)$ we avoid singularity because M_{00}^{out} can be zero by definition (Eq. (3)). The background value, that we are looking for, is given by $\operatorname{argmax} f(\mu_b \mid \hat{\mu}_{i,j})$. Because we use the Dual Annealing algorithm which can only find the global minimum of a function we work with the inverse objective function and minimize $-f(\mu_b \mid \hat{\mu}_{i,j})$ instead. The $\hat{\mu}_{i,j}$ is a parameter in this case and during minimization it is fixed for one specific time-point.

Minimizing the objective function

$$\underset{\mu_b \in \mathbb{R}^+}{\text{minimize}} \quad -f(\mu_b \mid \hat{\mu}), \tag{5}$$

allows us to determine the optimized background value $\widetilde{\mu_b}$ which we can use in Eq. (2) to calculate time-series of the moments quantities. Typical form of the objective function is shown in Figs. 1 and 2 for two particular days: 01.08.2008 and 06.09.2008 respectively.

We discuss two typical cases: first, MSF values inside the ASMA box are larger than outside of the ASMA box (Fig. 1) and second, there exist large MSF values outside of the ASMA box (Fig. 2). In the first case the ratio (Eq. 4) is low when μ_b is small compared to the values outside of the ASMA box, reflecting that subtraction of the background value doesn't impact the moments much but eventually M_{00}^{out} outside of the ASMA box starts to decrease compared to M_{00}^{in} when μ_b increases. Because the MSF values inside the ASMA box are dominating, it allows to reach such μ_b when M_{00}^{out} becomes zero (or almost zero)

https://doi.org/10.5194/egusphere-2025-1670
Preprint. Discussion started: 30 April 2025

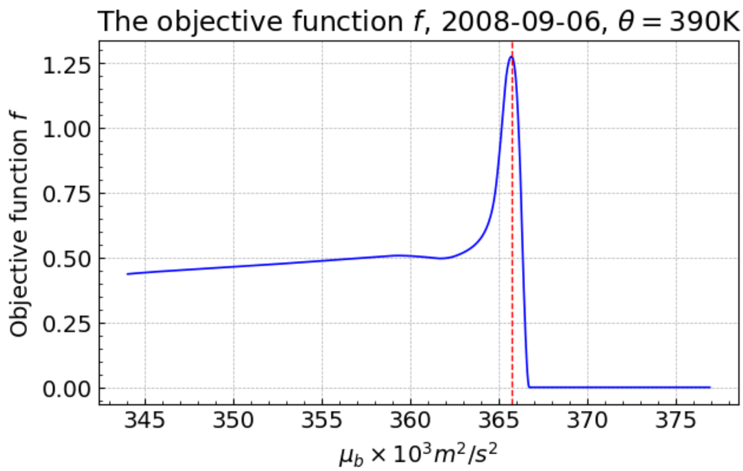

Figure 2. The objective function $f(\mu_b \mid \hat{\mu})$ depending on the background value μ_b for 9th September 2008 at 390 K with strong MSF values outside of the box. The maximum around $\widetilde{\mu_b} \approx 365.7$ is the optimized background value.

and only non-zero values are left inside of the box producing the high value of the objective function. Further with μ_b increase the M_{00}^{in} starts to decrease and eventually the ratio becomes zero when $\mu_b \geq \max|\hat{\mu}_{i,j}|$. This global maximum of the objective function is a property that allows us to see for such μ_b when the absolute vortex moment inside of the box is maximum while the values outside of the box are low or zero, hence sets the point of the optimized background value $\widetilde{\mu_b}$.

In the second case, if there is a strong circulation outside of the ASMA box the shape of the objective function is different but still preserves the global maximum and allows us to find such a $\widetilde{\mu_b}$ to encircle the anticyclone while also encircles what is present outside of the box.

After $\widetilde{\mu_b}$ is found, the absolute vortex moment (Eq. 2) can be used to define the ASMA boundaries as well as centroid position, the angle between the latitude axis and the major axis of the ASMA, aspect ratio and excess kurtosis (Appendix A) for each time-point. Sometimes even $\widetilde{\mu_b}$ preserves small noise outside of the box or another circulation is also present as was noted before, so to calculate the absolute vortex moment quantities only values inside of the ASMA box are considered. With this approach, we can exclude small noise outside the ASMA box or the impact of other monsoon systems.

At this point we can retrieve time-series of the moments quantities. First the $\widetilde{\mu_b}$ value is determined for each day at 12:00 UTC for the period from 1980 to 2023 and then all moments quantities are calculated following the description (see Appendix A). Our approach is fundamentally different compared to Manney et al. (2021) where only one single background value μ_b is used for each isentropic surface over the analysed time period from 1979 to 2018.

Our approach reduces number of points in time where the method used by Manney et al. 2021 cannot capture the ASMA boundary. The disadvantage of using a single background value for all points in time can be shown using Eq. 2. During the chosen time range (1980-2023) two cases might occur: $\min|\hat{\mu}_{i,j}| \gg \mu_b$ and $\max|\hat{\mu}_{i,j}| \lessapprox \mu_b$. The operation

https://doi.org/10.5194/egusphere-2025-1670
Preprint. Discussion started: 30 April 2025

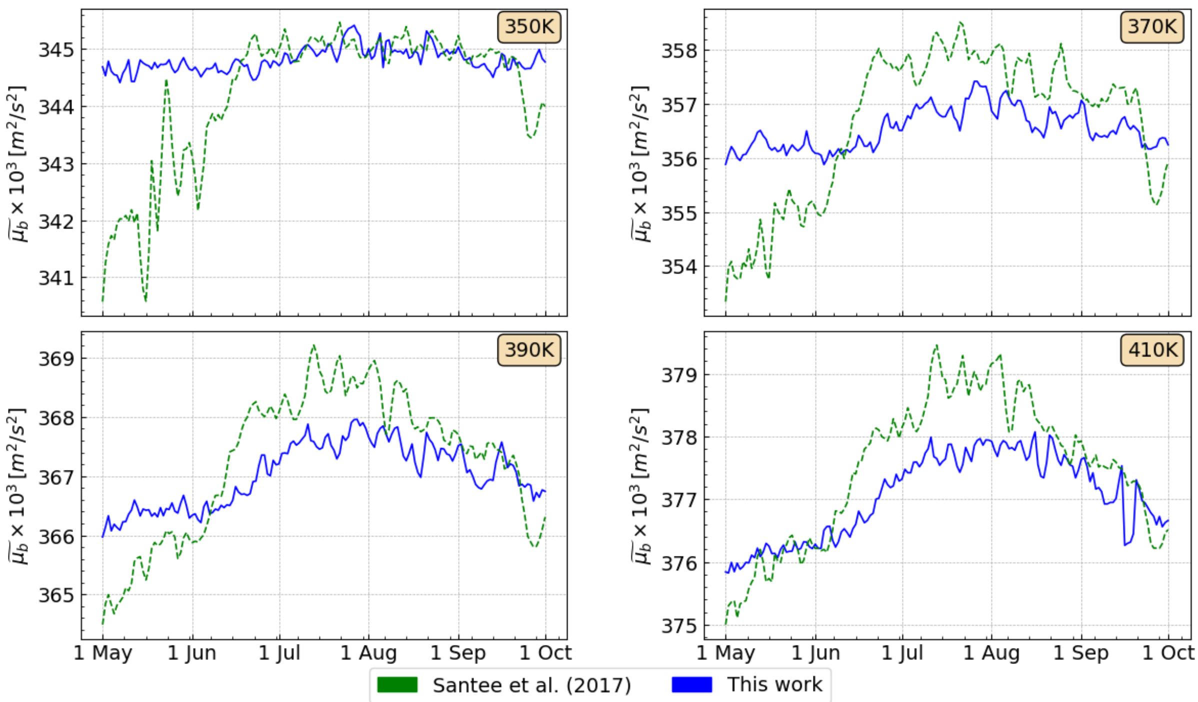

Figure 3. The Montgomery streamfunction optimized background values $\widetilde{\mu_b}$ using our approach (blue line) and according to Santee et al. (2017) (green dashed line) at 350, 370, 390 and 410 K for the Asian monsoon season 2023.

$$R_{i,j} := \hat{\mu}_{i,j} - \mu_b\,, \quad \text{for} \quad i = 0,\ldots,n-1 \quad \text{and} \quad j = 0,\ldots,m-1 \tag{6}$$

in Eq. 2 subtracts the background value μ_b from each grid point. In the first case, the background value μ_b might be not large enough to yield a boundary at all, in the second case the background value might cause the loss of information about optimized boundaries or even no information about the anticyclone at all.

In our approach, $\widetilde{\mu_b}$ is calculated for each point in time that yields optimized boundaries of the ASMA during the entire Asian monsoon season.

Manney et al. (2021) use a single background value per vertical level for the whole period analysed by Santee et al. (2017). Santee et al. (2017) took Montgomery streamfunction and wind speed values over a predefined region for June of a set of years and calculated a linear fit. The relationship then was used to retrieve MSF values that correspond to a chosen wind speed level (10 m/s at 370 and 390 K and 5 m/s at 350 and 410 K) on each isentrope ($\mu_b = 344.8, 356.5, 367.1, 377.3$ ($\times 10^3$ m^2/s^2) for 350, 370, 390 and 410 K respectively). To compare our method we used the Santee et al. (2017) methodology, but calculated μ_b for each time-point for each vertical level. The comparison to our approach is shown on Fig. 3 where we choose to show the Asian monsoon season 2023 (the other 43 years show similar time-series). During the developing (May-June) and break-up

https://doi.org/10.5194/egusphere-2025-1670
Preprint. Discussion started: 30 April 2025

(September) phases of the anticyclone, the Santee et al. (2017) method gives lower values than our method, which means that some unwanted noise is still preserved with the Santee et al. (2017) methodology. During the peak phase of the anticyclone the results of both methods are reversed: the Santee et al. (2017) approach gives higher values of the background value than value determined in this work, which leads to loosing some information on the edge of the anticyclone and shrinks its area at 370, 390 and 410 K. Our method shows $\widetilde{\mu_b}$ values for 350 K that have a small variation during the whole Asian monsoon season reflecting that at 350 K the ASMA does not exist. In contrast to the Santee et al. (2017) method that show an increase during the development of the ASMA and an decrease during the break-up. Our results are consistent with other methods such as the vorticity-based determination of the ASMA boundary that also found the ASMA at levels higher than 350 K (Ploeger et al. 2015).

The next step is to define the peak phase of the Asian monsoon anticyclone (referred to as "ASMA peak phase") to highlight the period of the anticyclone between the developing and break-up phases. In previous studies, different approaches were used to define the monsoon peak phase, very often a fixed time range was used, for example June-July-August (JJA) or July-August (JA) (e.g., Chen et al. 2021, Park et al. 2008).

Manney et al. (2021) use the methodology that is based on the area threshold. The ASMA peak phase is considered to begin (to end) when the anticyclone's area rises above (drops below) 1% of the area of the hemisphere for 20 consecutive days before (after) the start (end) date.

In our case using only the area time-series was not enough to obtain robust start (end) dates. Instead, we define the index by performing principal component analysis (PCA) over a set of quantities: the anticyclone's area, the optimized background value $\widetilde{\mu_b}$, pressure and potential vorticity. The last two were averaged in the ASMA box to obtain a single value per time-step. All quantities were normalized before performing PCA – by retrieving standard score ($\mathrm{score} = \frac{x-\overline{x}}{\sigma}$) for the period of 1980-2023. The ASMA peak phase is defined to start (end) when the index has been greater (lower) than 0 for 14 consecutive days.

To ensure that the ASMA box position is robust to adjustment we apply a sensitivity analysis by comparing a set of optimized background values of altered ASMA box position to the reference $\widetilde{\mu_b}$ (see Appendix B).

The proposed methodology of encircling the anticyclone allows us to perform the interannual analysis using the centroid latitude and longitude, excess kurtosis, angle, aspect ratio and the ASMA relative area. As was mentioned before the anticyclone's area was not calculated via absolute vortex moments which provides the equivalent area of the ellipse. Instead we calculate the area (km^2) of a polygon retrieved from the ASMA boundaries that is projected on the Earth surface and then take it as a fraction of the Northern hemisphere.

3 Variability of the Asian summer monsoon anticyclone

3.1 Horizontal distribution of the ASMA

The difference $R_{i,j}$ (Eq. 6) between the Montgomery streamfunction grid values ($\hat{\mu}_{i,j}$) and the optimized background $\widetilde{\mu_b}$ indicates the location of the ASMA (shown in Fig. 4) and is referred to as residual MSF. Figure 4 shows the mean residual MSF for 1980 to 2023 derived from 44 years of ERA5 $1^\circ \times 1^\circ$ reanalysis data from which the ASMA boundaries are inferred

https://doi.org/10.5194/egusphere-2025-1670
Preprint. Discussion started: 30 April 2025

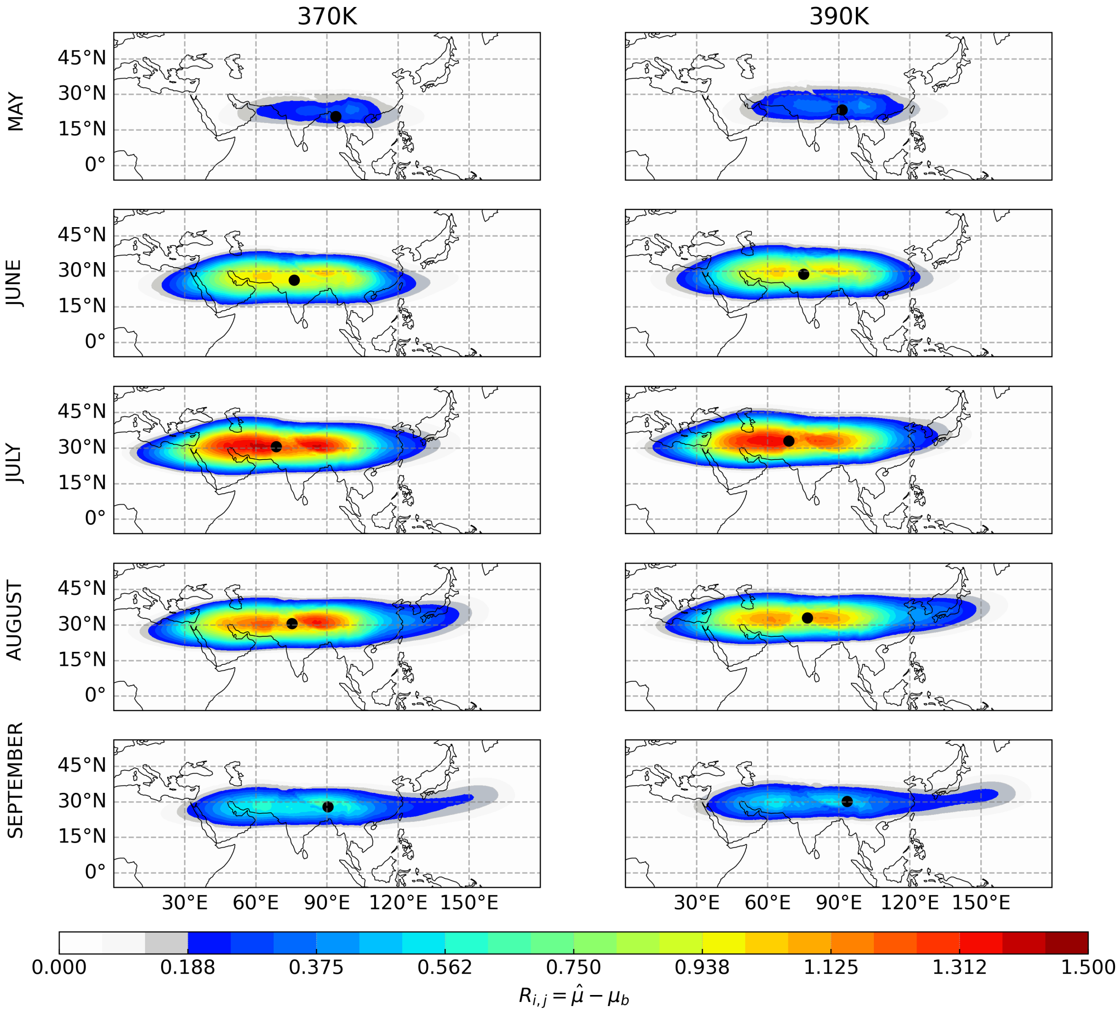

Figure 4. Mean residual MSF for 1980-2023 for the Asian monsoon anticyclone (the difference between MSF values and the background value) for each individual month from May to September (rows) at 370 and 390 K (columns).

230 and centroid position for 370 and 390 K isentropic surfaces (350 and 410 K are shown in Fig. C1 in the Appendix) for each month from May to September. Each row consists of individual months and the columns represent the vertical level. The mean residual MSF does not represent the optimized boundaries of the ASMA at any specific time-point and are used here only for a qualitative description of the ASMA development from pre-monsoon to post-monsoon.

https://doi.org/10.5194/egusphere-2025-1670
Preprint. Discussion started: 30 April 2025

Figure 4 shows that during May the ASMA starts to develop and settles over South Asia at 370, 390 and 410 K (shown in Fig. C1 in the Appendix). At 350 K (Fig. C1 in the Appendix), only a very weak anticyclone is indicated and temporarily separated into two parts demonstrating that the main ASMA is above 350 K.

Mean residual MSF values rise and fall through May-September and peak in July-August. Further, the position of the anticyclone changes during the ASMA peak phase. A northward shift is found at the beginning and a shift towards the tropics is found in the late ASMA phase.

From Fig. 4 we can see that starting in June the values tend to cluster around both sides relative to the centroid position, indicating a western part (Iranian mode) and eastern part (Tibetan Mode) of the anticyclone.

During July stronger values of the mean normalised MSF were found in the western part compared to the eastern part, even the area of the western part is larger in the climatological mean. This feature suggests a possible bimodality of the ASMA which is discussed in more detail in Sec. 3.2.

During break-up phase in September, the shape of the mean residual MSF is elongated and shrunk along latitude axis, indicating the break-up of the anticyclonic circulation. The temporal evolution of the ASMA during the monsoon season will be discussed in Sec. 3.3.

Figures 5, 6 and 7 show examples at 390 K of the ASMA boundaries, potential vorticity, wind velocity and corresponding moments quantities for three days during which relatively high absolute values of the angle and excess kurtosis were deduced. During 15.07.2017 at 390 K the anticyclone was titled counter-clockwise and the angle quantity is $-8.16°$, which can be observed in the corresponding time-series (Fig. 13). Figure 6 shows a positive angle ($3.37°$) because of the boundary curvature to the north around $60°E$. Fig 7 shows a splitting-like behavior of the anticyclone and how the excess kurtosis is enhanced (2.35) compared to the example on Fig. 5 where no splitting occurs.

In addition we provide a comparison of the boundary determined with our method and the Ploeger et al. (2015) PV-based transport barrier of the ASMA. Figure 8 shows the PV-based barrier as a blue dashed line and our boundary is denoted as a black line for 14.07.2022 at 370 K. Both methods capture the curvature of the northern side of the boundary around 80°E. The southern part is also aligned for the two methods and both follow wind velocity arrows. The Ploeger et al. (2015) boundary of the ASMA contains somewhat more noise compared to the boundary in this work and doesn't capture the western tail of the ASMA between $0°\mathrm{E} - 10°\mathrm{E}$. Using the Ploeger et al. (2015) method it is not always possible to determine a PV barrier on a daily scale, for this reason interpolated PV barrier is taken for comparison and illustrated in Fig. C2. While our method captures the boundary around $0°\mathrm{E} - 135°\mathrm{E}$ and aligns with wind velocity, the interpolated PV boundary is only able to encircle ASMA in range $90°\mathrm{E} - 135°\mathrm{E}$.

3.2 Bimodality and eddy shedding of the ASMA

Nützel et al. (2016) used seven reanalyses and found strong evidence of bimodality only in the obsolete reanalysis NCEP-R1 and no evidence in daily data (or limited evidence for monthly data) in more modern reanalyses. Nützel et al. (2016) identified the center of the ASMA using the data of the absolute zonal wind field and the geopotential field at 100 hPa (Zhang et al.

https://doi.org/10.5194/egusphere-2025-1670
Preprint. Discussion started: 30 April 2025

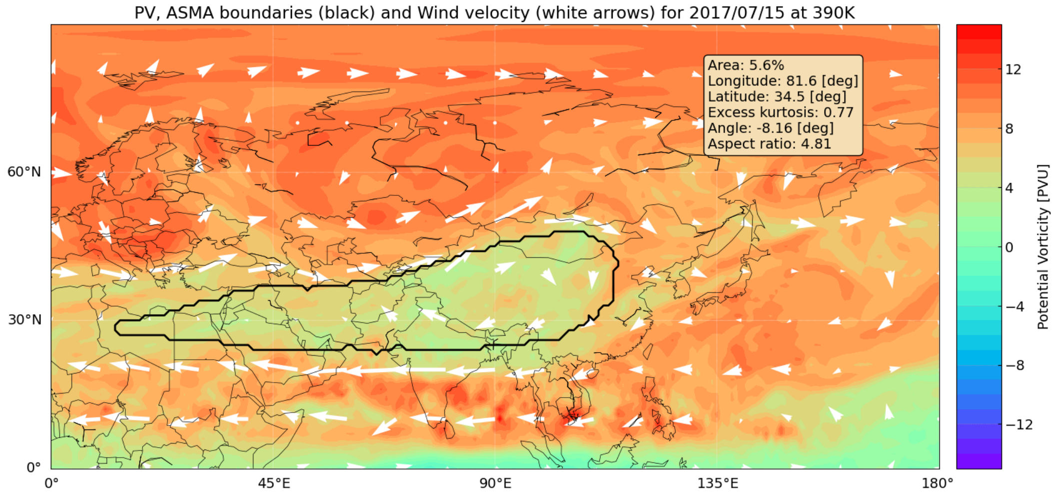

Figure 5. Horizontal plot of the ASMA boundaries (thick black line), potential vorticity (colormap), wind velocity (arrows) and corresponding moments quantities for 15.07.2017 at 390 K.

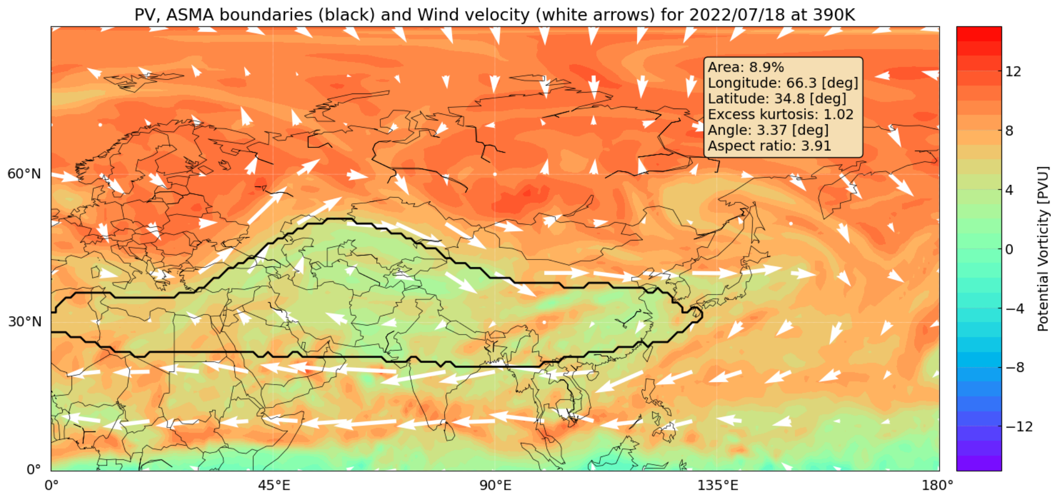

Figure 6. Horizontal plot of the ASMA boundaries (thick black line), potential vorticity (colormap), wind velocity (arrows) and corresponding moments quantities for 18.07.2022 at 390 K.

2002). Manney et al. (2021) used the MERRA-2, ERA-I and JRA-55 reanalyses and support the results of Nützel et al. (2016) for recent reanalyses.

However, our results show that the values of the mean normalised MSF are clustered in a western and eastern part of the ASMA at 370, 390 and 410 K between June and September (Fig. 4; Fig. C1) indicating a bimodality of the ASMA.

https://doi.org/10.5194/egusphere-2025-1670
Preprint. Discussion started: 30 April 2025

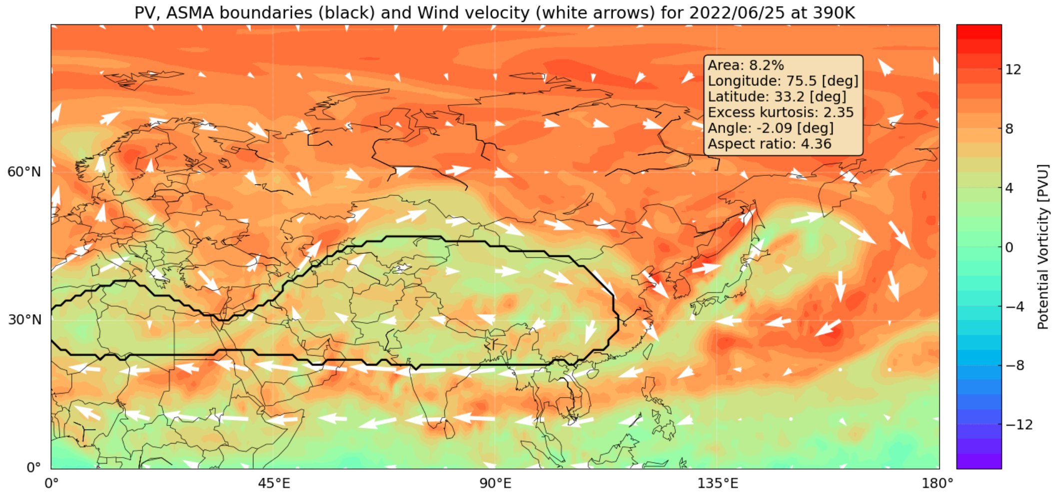

Figure 7. Horizontal plot of the ASMA boundaries (thick black line), potential vorticity (colormap), wind velocity (arrows) and corresponding moments quantities for 25.06.2022 at 390 K.

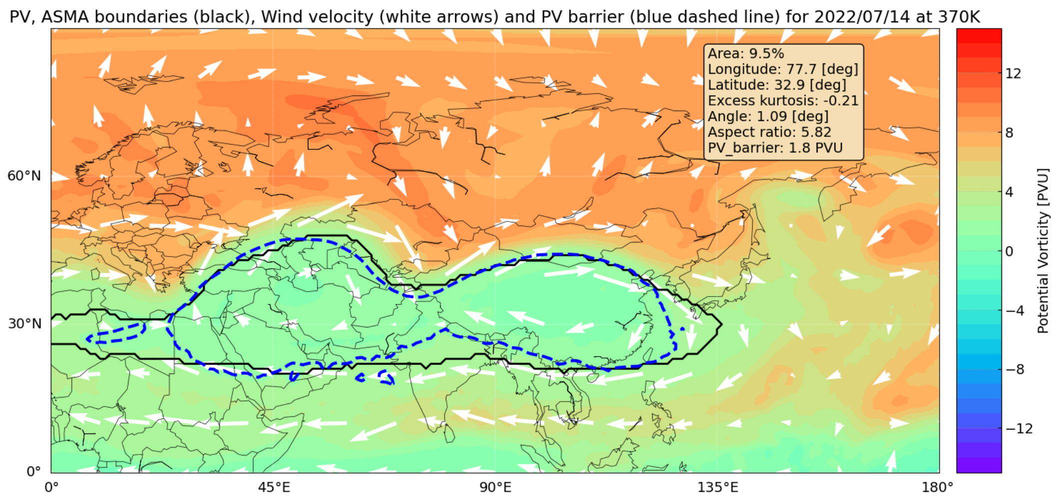

Figure 8. Horizontal plot of the ASMA boundaries (thick black line), potential vorticity colormap (`PV_MEAN` as defined in Ploeger et al. (2015)), wind velocity (arrows), PV barrier (blue dashed line) and corresponding moments quantities for 14.07.2022 at 370 K.

The temporal variability of the bimodality is analysed using Hovmöller diagrams at 370 and 390 K (Fig. 9 and 10; 350 and 410 K are shown in Figs. E1 and E2 in the Appendix). A zonal mean $R_{i,j}$ ($15°\mathrm{N} - 45°\mathrm{N}$) of the residual MSF for JJA of each year (1980-2023) (right) with corresponding optimized background values (left) are shown. High values of the zonal mean of the residual MSF indicate the longitudinal position of the ASMA. Because we are interested only in the positions, the $R_{i,j}$ values were normalized individually by dividing each year separately using its own maximum value. This way we can

https://doi.org/10.5194/egusphere-2025-1670
Preprint. Discussion started: 30 April 2025

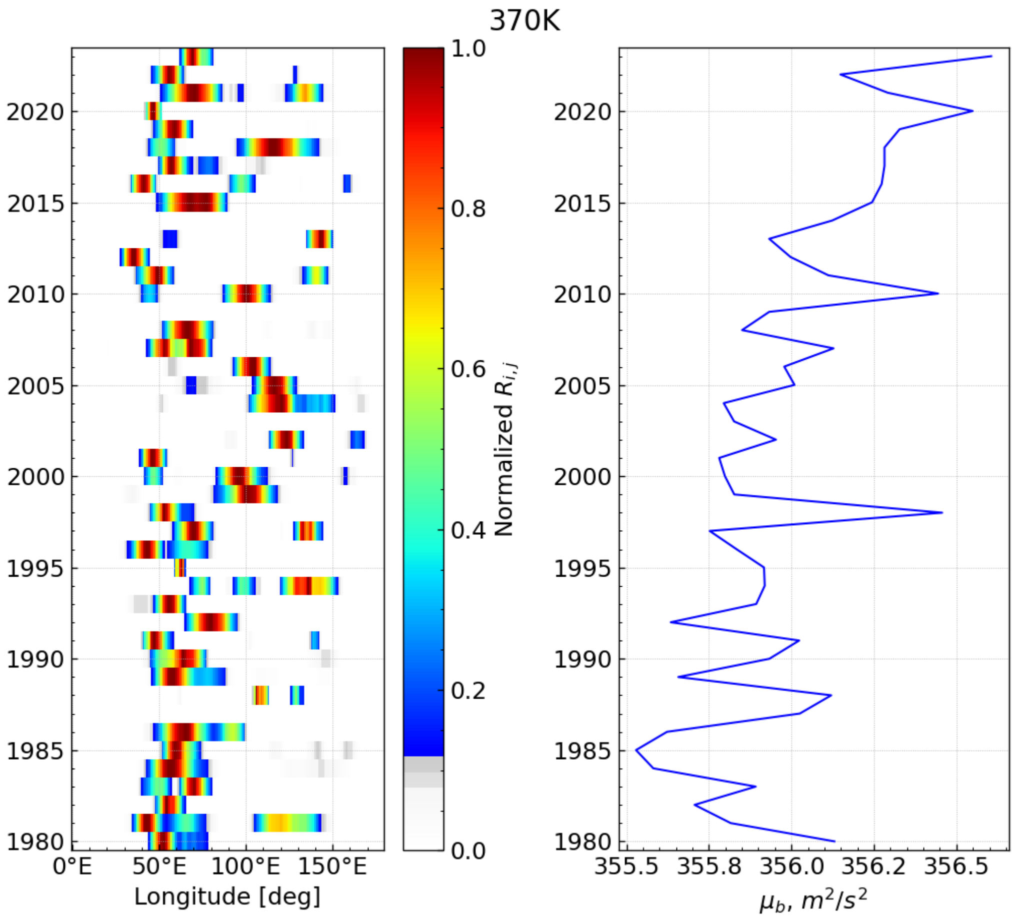

Figure 9. Mean JJA optimized background values (right) and Hovmöller diagram of normalized zonal mean (15°N – 45°N) of the residual MSF for 1980-2023 period at 370 K. Reddish colors indicate where the centroid longitudinal position of the ASMA tends to cluster.

qualitatively analyze the spatio-temporal distribution of residual MSF clusters and analyze a possible bimodality. For example, in 1981 the peak values are clustered around $45°E$ and simultaneously another cluster further to the east around $125°E$ is found (Fig. 10). A similar behavior we can see in 1986 but the clusters splits closer to around $80°E$ with the right part being weaker but still strong in terms of residual MSF having $\approx 85\%$ values of the maximum. One of the noticeable difference between the years is that during the 80s there were fewer splitting events than in the recent years.

To infer if the western and eastern part (modes) of the ASMA occur simultaneously or alternating (or both) we analyse the zonal mean residual MSF on a daily basis. The Hovmöller diagrams shows the possible bimodality of the ASMA in JJA, in addition we can quantify daily splitting of the residual MSF. Figure 11 shows the number of days per year when the normalized zonal $R_{i,j}$ is above the threshold (0.5) in both parts of divided longitudinal axis – the left (all positions $<$ mean_longitude)

https://doi.org/10.5194/egusphere-2025-1670
Preprint. Discussion started: 30 April 2025

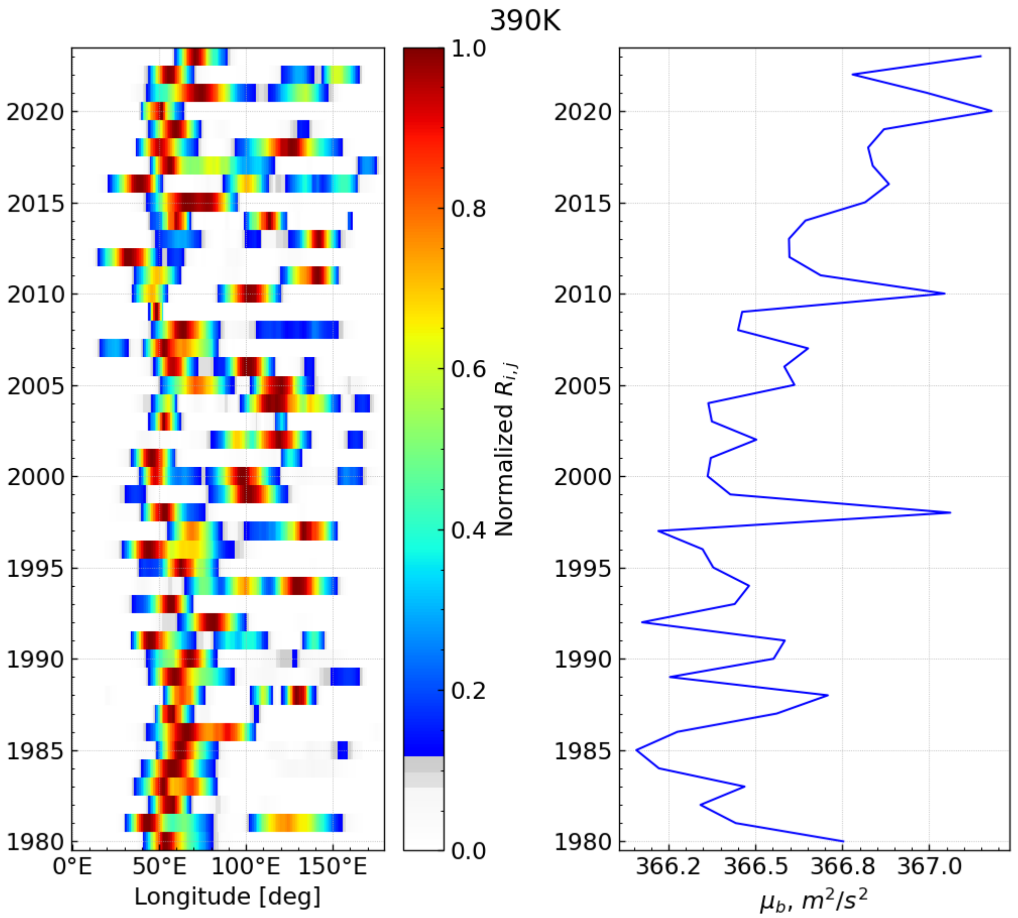

Figure 10. Mean JJA optimized background values (right) and Hovmöller diagram of normalized zonal mean ($15°\mathrm{N} - 45°\mathrm{N}$) of the residual MSF for 1980-2023 period at 390 K. Reddish colors indicate where the centroid longitudinal position of the ASMA tends to cluster.

285 and the right (all positions $>$ mean_longitude) parts. We calculate the average centroid longitude of the ASMA for each year and it serves as a logical line to divide the axis in two parts. If for each day the $R_{i,j}$ values above the threshold occurred in the both parts we count it as a bimodal day.

In Fig. 11 we can see that for the majority of the years the bimodality of the ASMA usually lasts for less than 10 days for May-September period at 370 K, however a larger number of days is found at 390 K (up to 18 days).

290 We presented three types of plots to show possible bimodality of the ASMA: climatological horizontal plots for $R_{i,j}$, Hovmöller diagrams of zonal $R_{i,j}$ during JJA for each year and number of days per year when zonal $R_{i,j}$ is above the threshold simultaneously in multiple positions. All of them show that there is a bimodality of the ASMA if we use our methodology to define the optimized background and residual MSF.

https://doi.org/10.5194/egusphere-2025-1670
Preprint. Discussion started: 30 April 2025

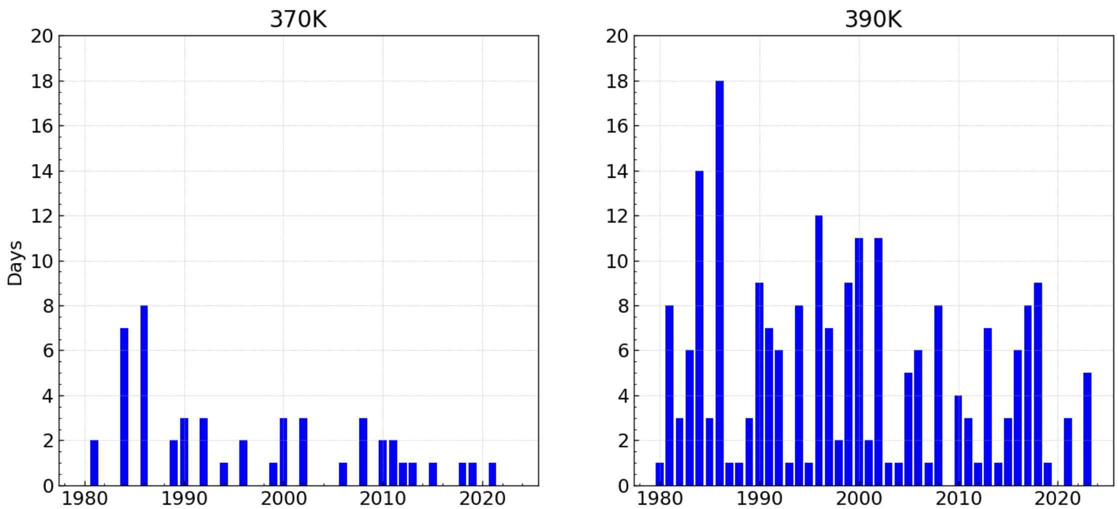

Figure 11. Number of days per year when normalized residual zonal mean $R_{i,j}$ is above the threshold (> 0.5) in both the western and eastern part at 370 K (left) and 390 K (right) indicating bimodality i.e., the simultaneous existence of two parts (modes) of the ASMA. The separation line that splits the western and eastern part is defined as average centroid longitude of the ASMA for the corresponding year.

3.3 Intraseasonal and interseasonal variability of the Asian summer monsoon anticyclone

Figures 12, 13 and 14 show the intraseasonal variability of the climatological mean (1980-2023) of the anticyclone's moments, namely the centroid position of the ASMA latitude and longitude, excess kurtosis, the angle and aspect ratio and, additionally, the relative area at 370 and 390 K (350 and 410 K are shown in Fig. D1,D2,D3 in the Appendix) from May to September. Moreover, we show individual time-series for 2017, 2022 and 2023 to highlight years when aircraft measurements inside the ASMA were conducted during the StratoClim (Stroh and StratoClim-Team 2025), the ACCLIP (Pan et al. 2024) and PHILEAS (Riese et al. 2025) aircraft campaigns respectively.

The intraseasonal variability of the centroid latitude position indicates a geographical northward shift of the ASMA until August and a subsequent southward shift towards the tropics afterwards. The centroid latitude time-series (Fig. 12, left) of the anticyclone is positioned between $10°N - 20°N$ in May at 370 and 390 K. During the ASMA peak phase the centroid position moves northward up until August and then starts to move to the south again. In September the centroid position is placed further northward than when it started near $20°N - 25°N$. The difference of the latitude centroid position for the years 2017, 2022 and 2023 to the climatological mean indicate the strong interseasonal variability of the ASMA. The northward movement of the ASMA is further to the north during 2022 than for 2023 for almost the whole May-September time-series at all vertical levels although the difference is small, only quickly at the beginning of August longitude centroid positions for both 2022 and 2023 were nearly the same. The year of 2017 usually better aligns with the climatology than 2022 and 2023.

https://doi.org/10.5194/egusphere-2025-1670
Preprint. Discussion started: 30 April 2025

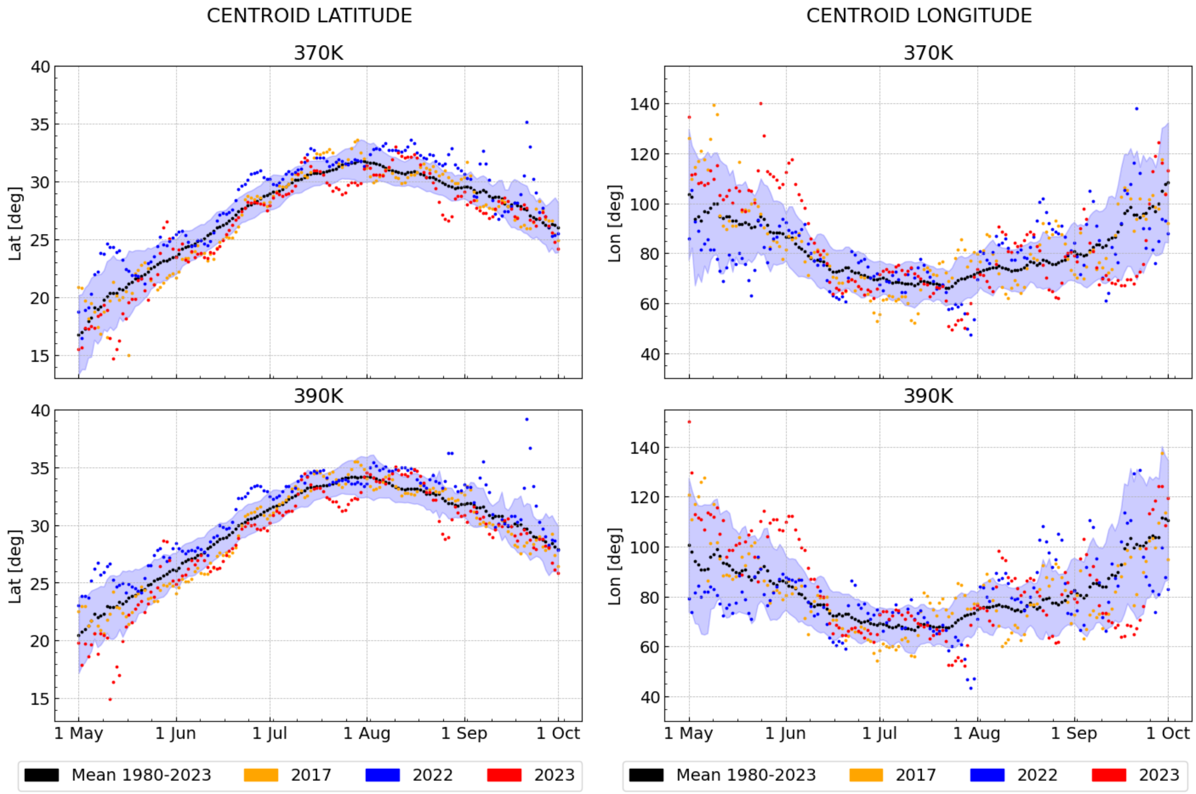

Figure 12. Climatological (1980-2023) time-series (black dots) of the centroid position of the ASMA latitude (left hand side) and longitude (right hand side), and individual years of 2017 (yellow dots), 2022 (blue dots) and 2023 (red dots) at 370 and 390 K. The lavender background denotes the standard deviation of the climatological data.

The intraseasonal variability of the centroid longitude position indicates a geographical westward shift of the ASMA until end of July and a subsequent eastward shift afterwards. The centroid longitude time-series (Fig. 12, right) of the anticyclone shows the evolution of the position start on the east near 150°E, eventually shifting to the west where it occupies the longitudinal band around 70°E at 370 and 390 K. After its peak, the position of the ASMA centroid is shifted to the east during the end of the monsoon season and returns to the location of 150°E in September. The difference of the longitude centroid position for the years 2017, 2022 and 2023 and the climatological mean indicates the strong interseasonal variability of the ASMA. Looking into highlighted years in June the position of the ASMA centroid longitude is shifted to the east in 2017 and 2023 more than in 2022 at all vertical levels with a maximum difference approximately 30°. The difference between the latitude centroid position for the years 2017, 2022 and 2023 and the climatological mean indicates the strong interseasonal variability of the ASMA.

Years 2017, 2022 and 2023 highlight a periodic nature of the ASMA area time-series when during June-August south-north ward oscillation as well as east-west oscillation are found similar as variabilities found in Asian summer monsoon rainfall (Goswami 2012).

https://doi.org/10.5194/egusphere-2025-1670
Preprint. Discussion started: 30 April 2025

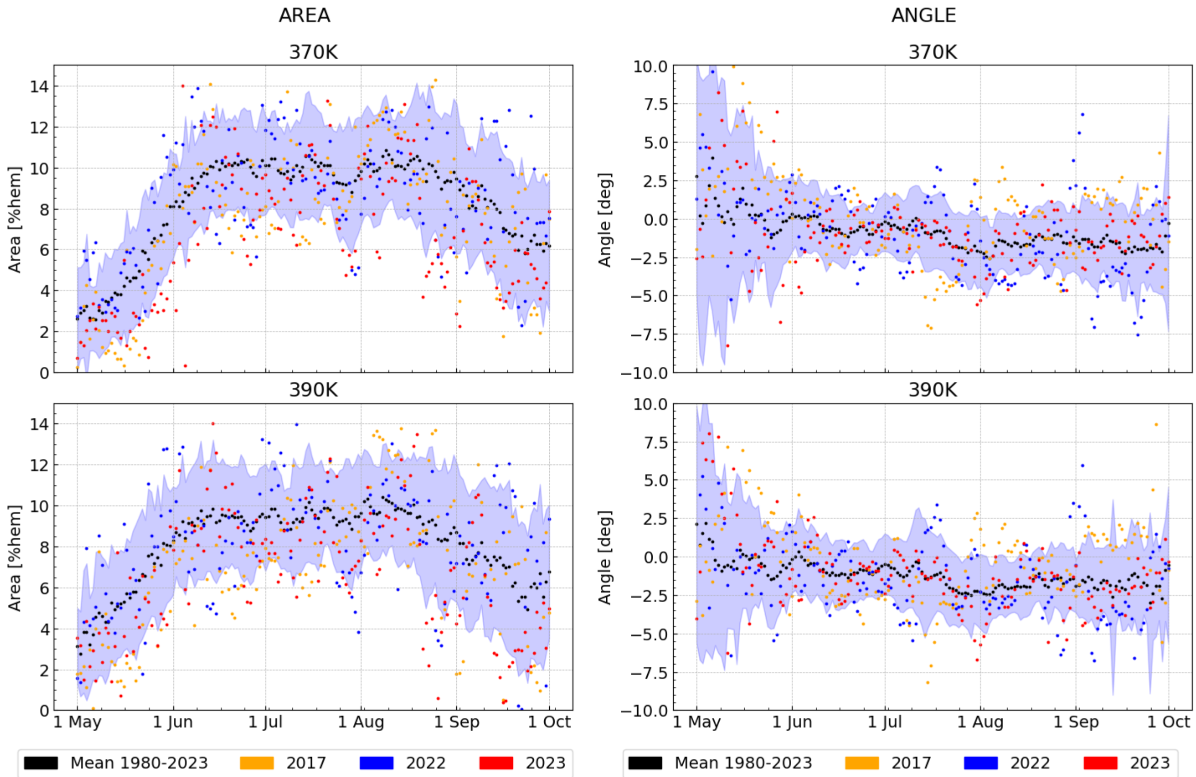

Figure 13. Climatological (1980-2023) time-series (black dots) of the ASMA area (left hand side) and angle (right hand side), and individual years of 2017 (yellow dots), 2022 (blue dots) and 2023 (red dots) at 370 and 390 K. The lavender background denotes the standard deviation of the climatological data.

The area of the ASMA (Fig. 13, left) is increasing during its development until mid-June, stays nearly constant in its peak-phase and starts to decrease end of August. In May the area of the ASMA is only nearly 2% of the area of the hemisphere and then gradually starts to increase. The steepest rise is seen at 370 K during mid of May. During the ASMA peak phase between June and September the ASMA area stays roughly the same at level of 10% of the hemisphere at 370, 390 and 410 K. At the beginning of September the area starts to decrease at 370 and 390 K, for 410 K the process starts earlier – in August.

The highlighted years (2017, 2022, 2023) generally tend to group around the climatology despite their higher variability. The values of the time-series are more robust at 370 and 390 K (Fig. 13) and the majority of the ASMA areas lie within one standard deviation of the climatology in contrast to 350 and 410 K (Fig. D2, left).

These oscillations are averaged out when considering the climatological time-series but a quick decline of the ASMA area can be seen at the end of July at all vertical levels. This decline in the ASMA area values varies between altitude, at 350 K the ASMA area decreases almost to zero for all highlighted years. During 2022 and 2023 the ASMA area cuts roughly by half from its climatological level at 370, 390 and 410 K.

https://doi.org/10.5194/egusphere-2025-1670
Preprint. Discussion started: 30 April 2025

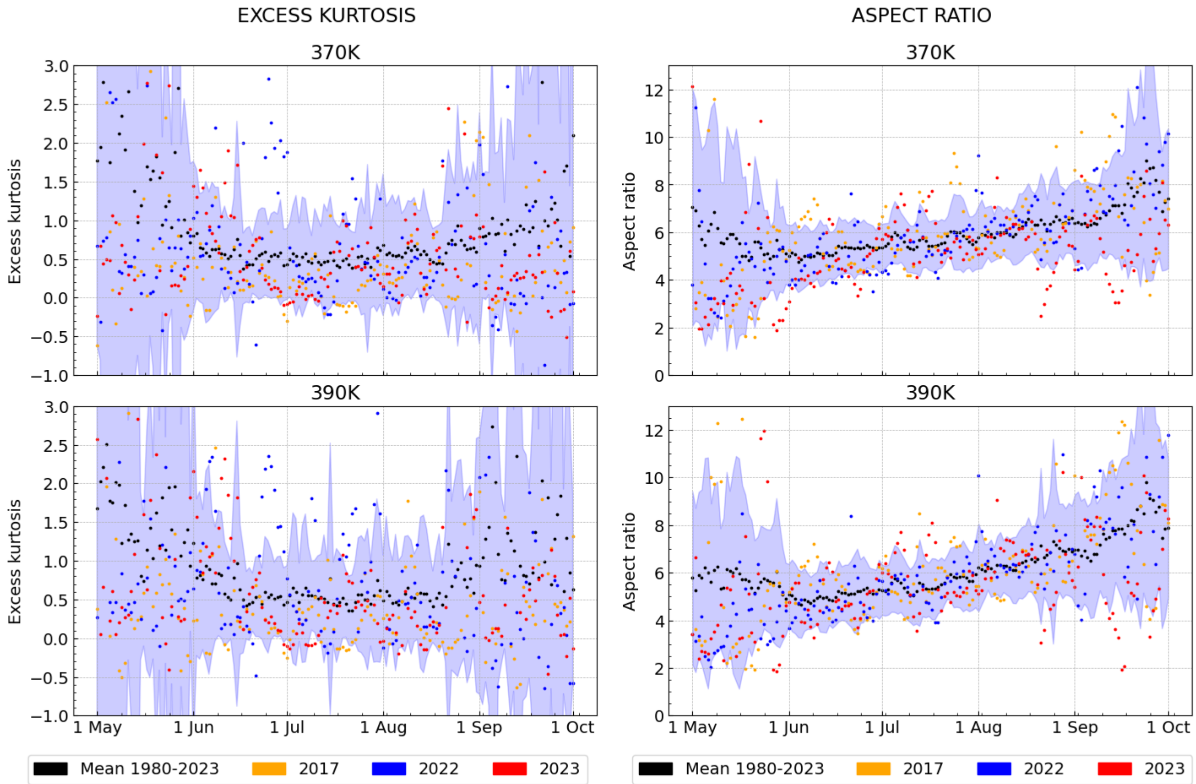

Figure 14. Climatological (1980-2023) time-series (black dots) of the ASMA excess kurtosis (left hand side) and aspect ratio (right hand side), and individual years of 2017 (yellow dots), 2022 (blue dots) and 2023 (red dots) at 370 and 390 K. The lavender background denotes the standard deviation of the climatological data.

The temporal evolution of the climatology of angles between the equatorial axis and the major axis of the ASMA ellipse are very low (around zero) indicating that the major axis of the ASMA is almost parallel to the equator during the monsoon season (Fig. 13, right). The individual years in contrast show low angle oscillations during the whole season. They have something similar to a phase shift relative to each other and that is why the climatological data are almost always equal to zero.

One relatively high deviation from zero can be seen in July 2022 at 390 K and 410 K when the angle decreases below zero at first but then rises above zero before stabilizing. A similar event was not found in 2017 and 2023.

Excess kurtosis (EK) measures the degree of splitting of the ellipsoid and therefore can serve as a metric for the bimodality (trimodality) of the ASMA (Fig. 14). During the developing phase of the ASMA up to until June and also during the break up phase after September the standard deviation of EK (and thus its variability) is higher than in the ASMA peak phase during the June-September period at all vertical levels because the anticyclone is not considered as stable. Overall EK serves as a good measurement of exceptional cases that the anticyclone is experiencing, especially when it is more than a single data point that has strong deviation from climatology values but a set of points that smoothly form a parabolic shape. Such peaks usually

https://doi.org/10.5194/egusphere-2025-1670
Preprint. Discussion started: 30 April 2025

filtered out from the climatological values during averaging and they are better represented in individual years. The temporal evolution of the EK during 2022 shows that in June-September period there are more splitting like events than in 2023 at 390 K.

The aspect ratio (Fig. 14, right-hand side) is the ratio between major and minor axis of the ellipse and quantifies its elongation. During the ASMA peak phase the aspect ratio is between ∼1 and 10 at all vertical levels. Progressing through the season both the climatology and individual years show a good alignment of slowly increasing aspect ratio indicating that the anticyclone is stretching with time in west-east longitudinal direction. Comparing individual years it can be noted that between July and August there are a couple of rapid elongations for 2017 and 2023 at 370, 390 and 410 K. For 2022 there is only one rapid increase of the aspect ratio during late June at all vertical levels except 350 K.

Figures 12,13 and 14 show a good overall agreement with the results of Manney et al. (2021) study. Our method gives us hints about the ASMA's evolution between May and September despite a relatively strong variability. Both centroid latitude and longitude show similar temporal evolution as the Manney et al. (2021) findings. The aspect ratio is also increasing with time in both studies. Although the area of the ASMA occupies around 10% of the hemisphere in the beginning of August in our results and Manney et al. (2021) (MERRA-2), the shape of the time-series is more flat in this work during the peak phase of the ASMA compared to Manney et al. (2021). Manney et al. (2021) find a parabolic-like shape due to differences in the methodologies. Our method keeps the moment inside a defined ASMA box as large as possible until the objective function's minimum, that solely relies on MSF values, change the optimized background value. The moments inside the box relates to the area enclosed by the boundaries and that's why we see it is kept almost flat during the ASMA peak phase. Because we provide the individual years in addition to climatological time-series, our results show oscillations of excess kurtosis and angle quantities compared to Manney et al. (2021), which highlights more details about ASMA behavior.

3.4 Duration of the ASMA peak phase

To determine the start and end dates of the ASMA peak phase, we use the similar approach as Manney et al. (2021) (the ASMA peak phase starts (end) when the area is greater (lower) than 1% of the hemisphere for 20 consecutive days). However, here we use in addition further quantities describing the ASMA, namely pressure, PV, optimized background values $\widetilde{\mu_b}$ and ASMA area. The time-series of the index was calculated using PCA technique (see Sec. 2). Then we use a threshold for the index (0.0) to find two points on the index time-series that denote the start and end dates. Fig. 15 shows the time development of the start dates, end dates and the duration of the peak phase of the Asian summer monsoon anticyclone at three different levels of potential temperature. Each row on Fig. 15 denotes the vertical level and each column is for the anticyclone start date, end date and the duration in days ($end - start + 1$) respectively.

Manney et al. (2021) show that the anticyclone's peak phase tends (1979-2018) toward earlier formation, later break-up and longer duration at 350, 370, 390 and 410 K, with much larger trends at the lower levels. Our calculations (Fig. 15) show similar results at 370, 390 and 410 K (we do not provide the data for 350 K because this level is below the main anticyclone). We found the largest trends at 370 K. The end dates of the ASMA peak phase are shifted to later dates at all vertical levels. The trends for both start and end dates affect the duration of the ASMA peak phase which increases at all vertical levels, providing the

https://doi.org/10.5194/egusphere-2025-1670
Preprint. Discussion started: 30 April 2025

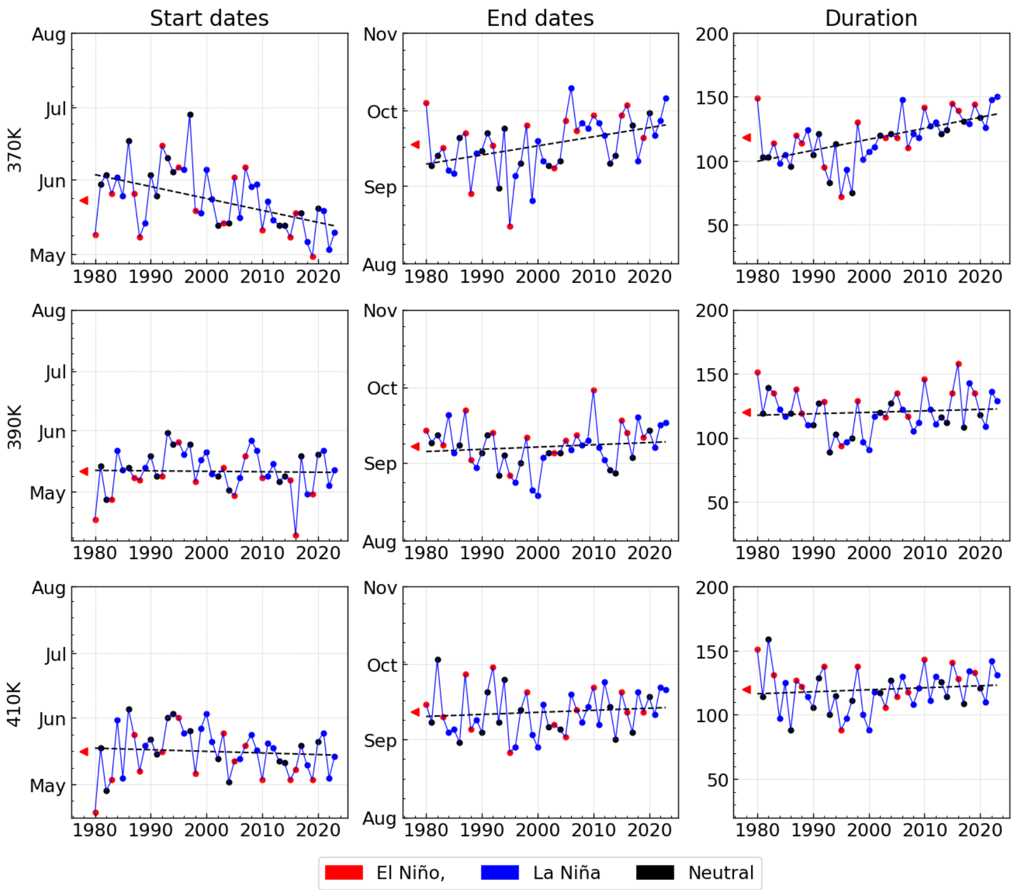

Figure 15. Start (left), end (middle) dates and the duration in days (right) of the ASMA peak phase at 370, 390 and 410 K. The red triangle denotes the mean value. Red colored circles correspond to El Niño years, blue to La Niña years and black one are neutral years (related to DJF, from the winter before the considered monsoon period).

information about a significant expansion of the ASMA peak phase in time, adding around 40 days in duration at 370 K and around 10 days at 410 K.

The coloring of individual years according to El Niño/La Niña suggests that there is some impact of ENSO on the duration of the ASMA peak phase at 370, 390 and 410 K. In general during El Niño years the ASMA peak phase is longer than during La Niña years but further analysis is needed to correlate the events.

https://doi.org/10.5194/egusphere-2025-1670
Preprint. Discussion started: 30 April 2025

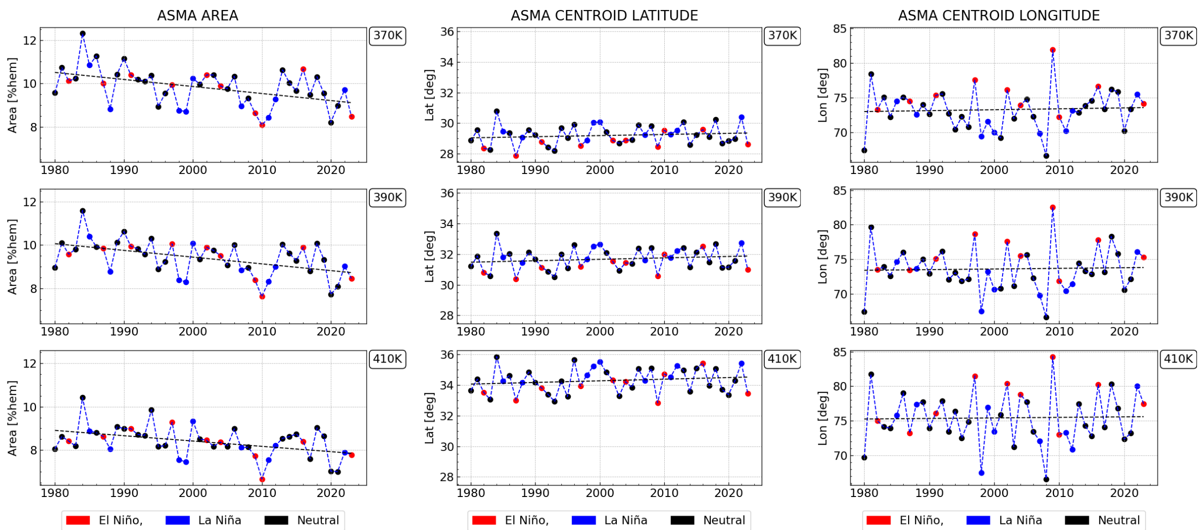

Figure 16. Trends of the ASMA area, centroid latitude and longitude for JJA based on ERA5 reanalysis. Color marks ENSO type of a year based on ONI index (using DJF, from the winter before the considered monsoon period). The year is marked as El Niño if the index is $> 0.5°C$, La Niña if the index is $< 0.5°C$, otherwise the year is marked as neutral.

3.5 Interannual trends of the ASMA area and location

We provide trends of the ASMA area, centroid latitude and longitude over 1980-2023 in JJA (Figure 16). The interannual variability of the ASMA area in JJA has only a few high outliers (e.g., in 1984) over the period 1980-2023. In contrast to Manney et al. (2021) the trend lines for 370, 390 and 410 K have a negative or near zero slope. To exclude the possibility that our trends might be different compared to Manney et al. (2021) as a different reanalysis is used, we repeated the methodology from Manney et al. (2021) and applied it to the ERA5 reanalysis. The results are shown in Fig. 17. The trend lines have positive slopes indicating that the area increases over 44 years (1980-2023); thus positive trends are found similar as in Manney et al. (2021) confirming that the difference between our results and those by Manney et al. (2021) is not caused by using a different reanalysis. The negative slopes on Fig. 16 for ASMA area are purely because of the used methodology that rely on individual background values instead of fixing one value per vertical level. If we don't fix the background value but instead try to find the optimized one based on the introduced objective function it leads to the ASMA area decreasing over the same period. If we look at the area time-series (Fig. 13, left), we notice that during June-August the area is almost flat in contrast to the findings by Manney et al. (2021). The ASMA area in JJA is averaged for each year and shown on Figure 16. It seems to give us an information that the area is decreasing. Manney et al. (2021) use a single background value per vertical level, hence the increase in area might be because of the spread of the higher MSF values in the region and the extent of area increase depends on the

https://doi.org/10.5194/egusphere-2025-1670
Preprint. Discussion started: 30 April 2025

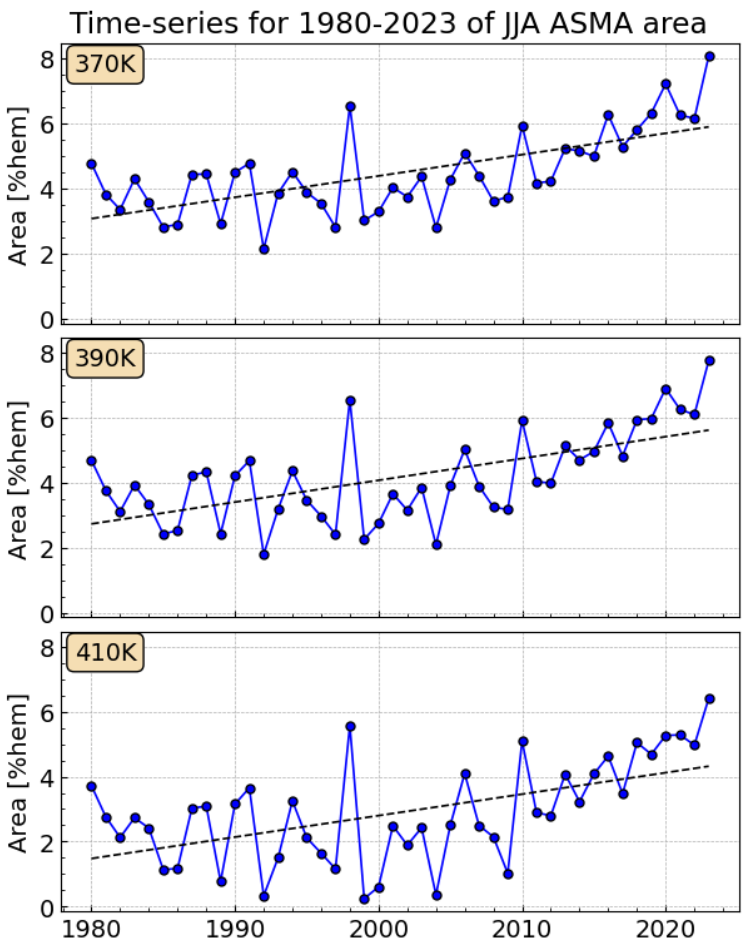

Figure 17. Same as Fig. 16 (left), but using the methodology by Manney et al. (2021).

chosen fixed MSF value. Our findings compared to Manney et al. (2021) show that the calculation of the change in the ASMA area over time depends in detail on the used methodology.

During El Niño years, the ASMA centroid is somewhat shifted towards the east and to the tropics and ASMA area size seems not to be correlated to ENSO at 370, 390 and 410 K. Manney et al. (2021) report similar conclusions for correlation between MEI (Multivariate ENSO Index) and ASMA area and centroid position.

4 Conclusions

We introduced a novel method based on the absolute vortex moments that is used to define boundaries of the Asian summer monsoon anticyclone. This method allows the interannual variability of the anticyclone and possible trends to be analysed. The method makes it possible to describe the ASMA on individual days from its formation phase in May-June, during the

https://doi.org/10.5194/egusphere-2025-1670
Preprint. Discussion started: 30 April 2025

peak phase to its break-up phase in September. In this work, the most recent ECMWF reanalysis ERA5 is used in contrast to previous studies (e.g., Manney et al. 2021) using earlier reanalyses (MERRA-2, ERA-Interim, JRA-55) having lower spacial resolution. The ASMA was analysed over a time period covering 44 years (1980-2023) on selected isentropic surfaces (370 and 390 K; 350 and 410 K are shown in Appendix C). In addition to climatological mean values over 44 years we investigate the anticyclone's behavior during individual years – 2017, 2022 and 2023 – when the aircraft campaigns StratoClim, ACCLIP and PHILEAS were conducted, respectively, in the region of the ASMA.

Our method shows good overall agreement with studies employing a PV-based boundary of the monsoon anticyclone but can be applied to individual points in time. Using the method we were able to identify bimodality (both on daily and seasonal time scales) of the ASMA in contrast to some previous studies.

Our analysis shows the qualitative spatial evolution of the ASMA on fixed levels of potential temperature (350, 370, 390 and 410 K). The distribution of the difference $R_{i,j}$ between the Montgomery streamfunction grid values ($\hat{\mu}_{i,j}$) and the optimized background $\widetilde{\mu_b}$ highlights climatological regions where the ASMA is occurring during corresponding months. At 370, 390 and 410 K the distribution is similar. When the anticyclone starts to form in May all vertical levels show a higher aspect ratio than during the peak phase. We show that horizontal plots of the residual MSF values provide the information about splitting-like behavior of the anticyclone in July, August and September in contrast to other studies that have not shown ASMA bimodality. With our new method and using the ERA5 reanalysis, we can confirm a bimodality of the ASMA in contrast to previous work.

The moments analysis provides a quantitative method based on six quantities using which we build spatio-temporal characteristics of the ASMA: the centroid latitude and longitude, excess kurtosis, angle, aspect ratio and area.

The time-series show that:

- The area of the ASMA increases gradually during May-June at 370, 390 and 410 K with the steepest rise seen at 370 K during mid of May. Individual years show an essential area drop at the beginning of August.

- South-north shift of the centroid position of the ASMA oscillates during the season and tends to shift poleward with vertical level. Individual years when campaigns were performed (2017, 2022 and 2023) are close to the climatology but the anticyclone tends to reside more northward during 2022 than in 2023.

- East-west shift evolves during the season, it has a minimum near 50°E at all vertical levels. The time-series of the centroid longitude starts and ends around 100°E. There is a significant difference between 2022 and 2023 in end of May and beginning of June. The ASMA is shifted more to the east during 2022 and the difference is around 30° compared to 2022 at all vertical levels.

- The excess kurtosis of the ASMA is near zero for the climatology but has distinct spikes in individual years indicating a splitting-like behavior showing bimodality and shedding events.

- On average the angle of the ASMA relative to the equator is near zero, but individual years oscillate and have shifted relative to each other.

https://doi.org/10.5194/egusphere-2025-1670
Preprint. Discussion started: 30 April 2025

– The aspect ratio of the ASMA has higher standard deviation during formation and break-up phase indicating its instability. During the whole season the values show a linear growth of the aspect ratio at all vertical levels. There is a shrinking and elongation effect that can be seen in individual years, especially in 2023.

Using the novel method, we determine start and end dates of the ASMA and thus its duration in days. The starting dates for the ASMA peak phase are between May-June. The end dates are in between September and October at 370, 390 and 410 K. The overall duration of the ASMA peak phase is around 120 days and has increased in recent years. The slopes of the trend lines suggest that the ASMA peak phase tends to start earlier and end later especially at lower altitudes over the period from 1980 to 2023 the monsoon period extended by ~ 10 (at 410 K) and ~ 40 (at 370 K) days. These findings are consistent with previous studies (Manney et al. 2021).

Interannual trends for 1980-2023 were determined for the anticyclone's area, centroid latitude and longitude. The area shows a decline over this period for all vertical levels. This results contradicts previous studies and is caused by the method itself; an impact of the used reanalysis could be excluded. Our findings show that the ASMA centroid position depends on ENSO. During El Niño (La Niña) years, the ASMA centroid is somewhat shifted towards the east (west) and to the tropics (mid-latitudes).

Overall, the new proposed method shows a straightforward way to calculate the moments quantities with reduced noise. The chosen methodology allowed us to conduct the robust analysis which gave us similar results with previous studies for centroid position, aspect ratio seasonal time-series and start and end dates of the ASMA. In addition our method highlighted differences in the interannual changes of the ASMA area that decreases compared to Manney et al. (2021) and allowed a possible bimodality of the ASMA to be analysed. Our new approach to describe the ASMA and its boundaries can be used on any time scale, choosing individual days or specific hours as well as climatological time scales of several decades to analyse previous or future possible changes of the Asian monsoon anticyclone caused by climate change.

https://doi.org/10.5194/egusphere-2025-1670
Preprint. Discussion started: 30 April 2025

Appendix A: The quantities retrieved using the absolute vortex moment

Using Eq. (3) Matthewman et al. (2009) define the equivalent ellipse by its centroid position $(\overline{x}, \overline{y})$, its angle of orientation ψ and its aspect ratio r:

$$(\overline{x}, \overline{y}) = \frac{1}{M_{00}}(M_{10}, M_{01}). \tag{A1}$$

To define ψ and r Matthewman et al. (2009) introduce the relative vortex moment:

$$J_{kl} = \int\int [\hat{\mu}_{i,j} - \mu_b](x - \overline{x})^k (y - \overline{y})^l dx\, dy, \tag{A2}$$

then

$$\psi = \frac{1}{2}\tan^{-1}\left(\frac{2J_{11}}{J_{20} - J_{02}}\right), \tag{A3}$$

$$r = \left|\frac{(J_{20} + J_{02}) + \sqrt{4J_{11}^2 + (J_{20} - J_{02})^2}}{(J_{20} + J_{02}) - \sqrt{4J_{11}^2 + (J_{20} - J_{02})^2}}\right|^{1/2}, \tag{A4}$$

and

$$\kappa_4 = M_{00}\frac{J_{40} + 2J_{22} + J_{04}}{(J_{20} + J_{02})^2} - \frac{2}{3}\left[\frac{3r^4 + 2r^2 + 3}{(r^2 + 1)^2}\right]. \tag{A5}$$

Appendix B: Sensitivity analysis

As was mentioned earlier, the ASMA box was defined as a region of ASMA occurrence and its position was introduced on our empirical knowledge where the Asian summer monsoon anticyclone can be found. To ensure that our approach is robust to adjustment of the latitude-longitude box position we apply a sensitivity analysis. The strategy is as follows: using Eq. 4 we consider one specific $\hat{\mu}_{i,j}$ but instead adjusting the ASMA box position by 1° starting from (0°N-90°N 0°E-180°E) until (−90°S-0°N 180°E-1°W) and retrieving $\widetilde{\mu_b}$ for each ASMA box. Figure B1 shows a distribution of the $\widetilde{\mu_b}$ with corresponding latitude-longitude shift. ΔLon, ΔLat axes show how many degrees are added to the ASMA box. As can be seen, the crossed region marks the range of step-sizes that area safe to add to the ASMA box while preserving the original $\widetilde{\mu_b}$ (using the ASMA box from the methodology). The range of ΔLon, ΔLat are within $0-20$ degree to the south and $0-40$ degree to the east confirming that our approach is robust relative to a fluctuation of the position of the ASMA box.

https://doi.org/10.5194/egusphere-2025-1670
Preprint. Discussion started: 30 April 2025

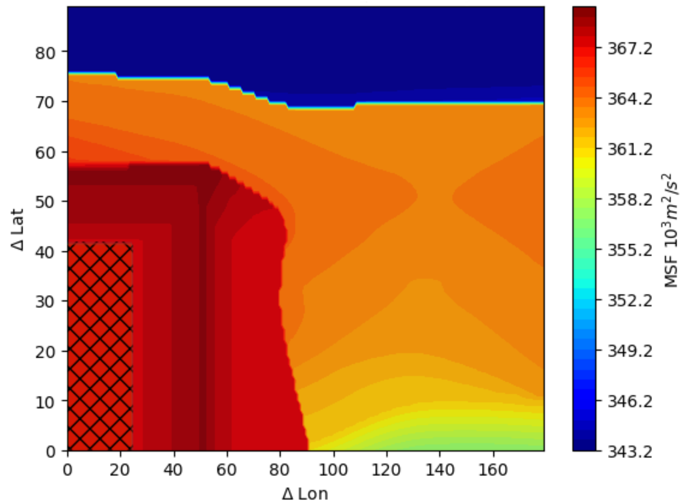

Figure B1. Sensitivity results of the latitude-longitude shift of the ASMA box and corresponding $\widetilde{\mu_b}$ using the MSF values from 01.08.2023 at 390 K. Crossed region highlights values within original background value ± 0.01.

Appendix C: Climatology of the horizontal distribution plots

The distribution $R_{i,j}$ at 350 K has no information in May at 350 K telling that the anticyclone has only started to form and it's residual values are negligible on the chosen scale. Overall during the season $R_{i,j}$ is small at 350 K compared to the rest of vertical levels. The values of $R_{i,j}$ at 410 K are stronger also smaller than 370 and 390 K.

https://doi.org/10.5194/egusphere-2025-1670
Preprint. Discussion started: 30 April 2025

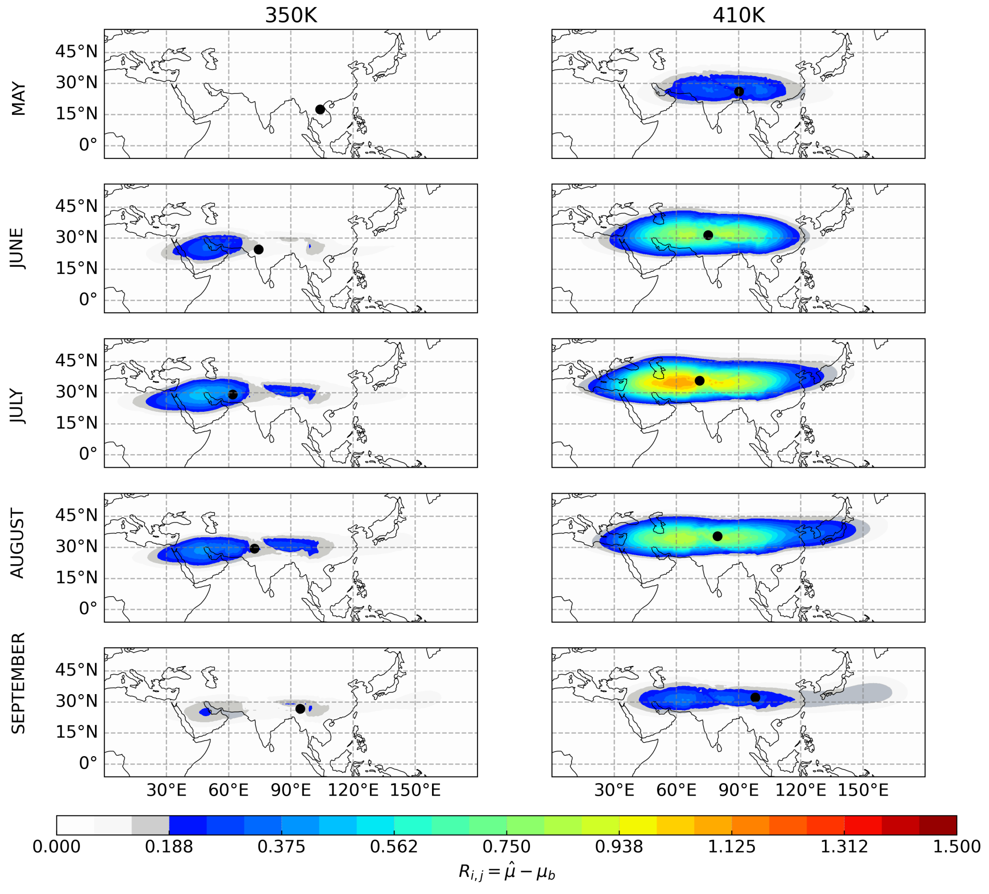

Figure C1. Mean residual MSF for 1980-2023 for the Asian monsoon anticyclone for each individual month from May to September (rows) at 350 and 410 K (columns).

https://doi.org/10.5194/egusphere-2025-1670
Preprint. Discussion started: 30 April 2025

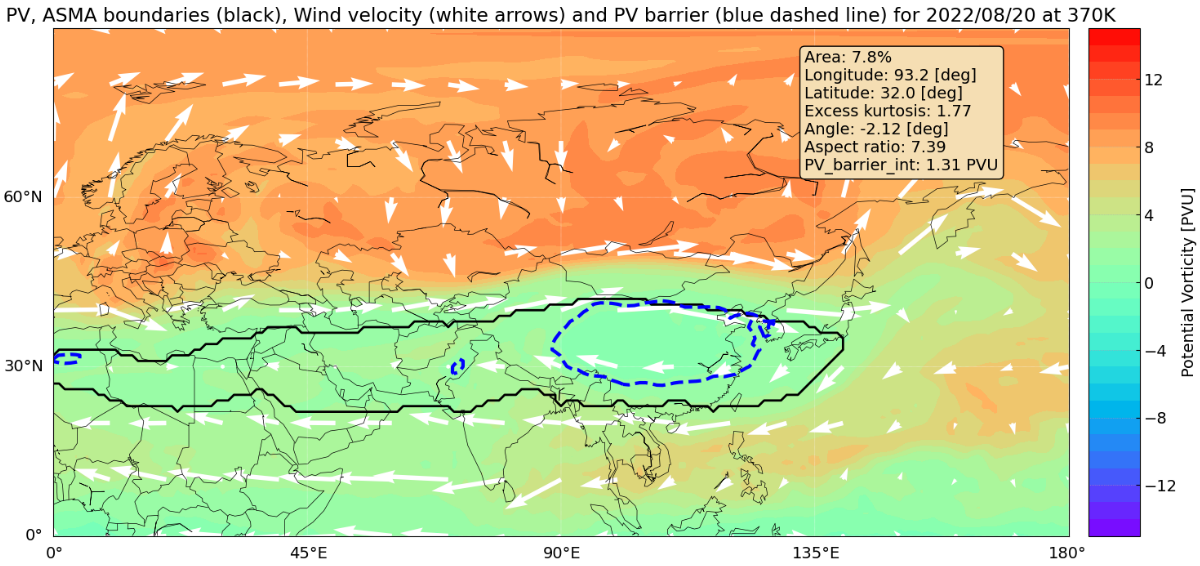

Figure C2. Horizontal plot of the ASMA boundaries (thick black line), potential vorticity colormap (`PV_MEAN` as defined in Ploeger et al. (2015)), wind velocity (arrows), interpolated PV barrier (blue dashed line) and corresponding moments quantities for 20.08.2022 at 370 K.

485 Appendix D: Climatological time-series of the ASMA moments quantities at 350 and 410 K

The moments quantities of the ASMA at 350 and 410 K overall behave similar to 370 and 390 K but the standard deviation at 350 and 410 K are higher. Excess kurtosis which shows the splitting-like behavior has more deviations at 410 K than 370 and 390 K and it does not serve as a reliable variable for 350 K. Similar can be seen with the angle quantity where higher tilting is presented at 350 and 410 K than 370 and 390 K. The area of the ASMA is usually smaller at 350 and 410 K and also have higher standard deviation.

https://doi.org/10.5194/egusphere-2025-1670
Preprint. Discussion started: 30 April 2025

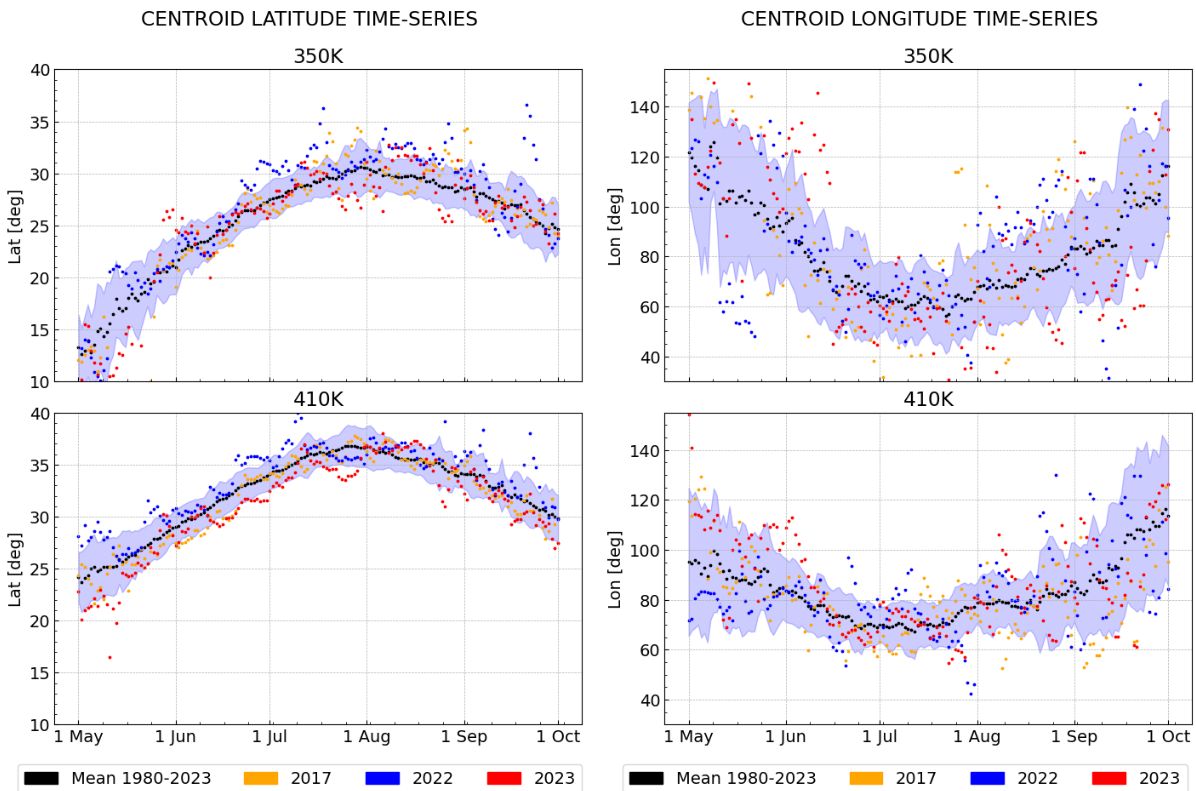

Figure D1. Climatological (1980-2023) time-series (black dots) of the ASMA centroid latitude (left hand side) and longitude (right hand side), and individual years of 2017 (yellow dots), 2022 (blue dots) and 2023 (red dots) at 350 and 410 K. The lavender background denotes one standard deviation of the climatological data.

https://doi.org/10.5194/egusphere-2025-1670
Preprint. Discussion started: 30 April 2025

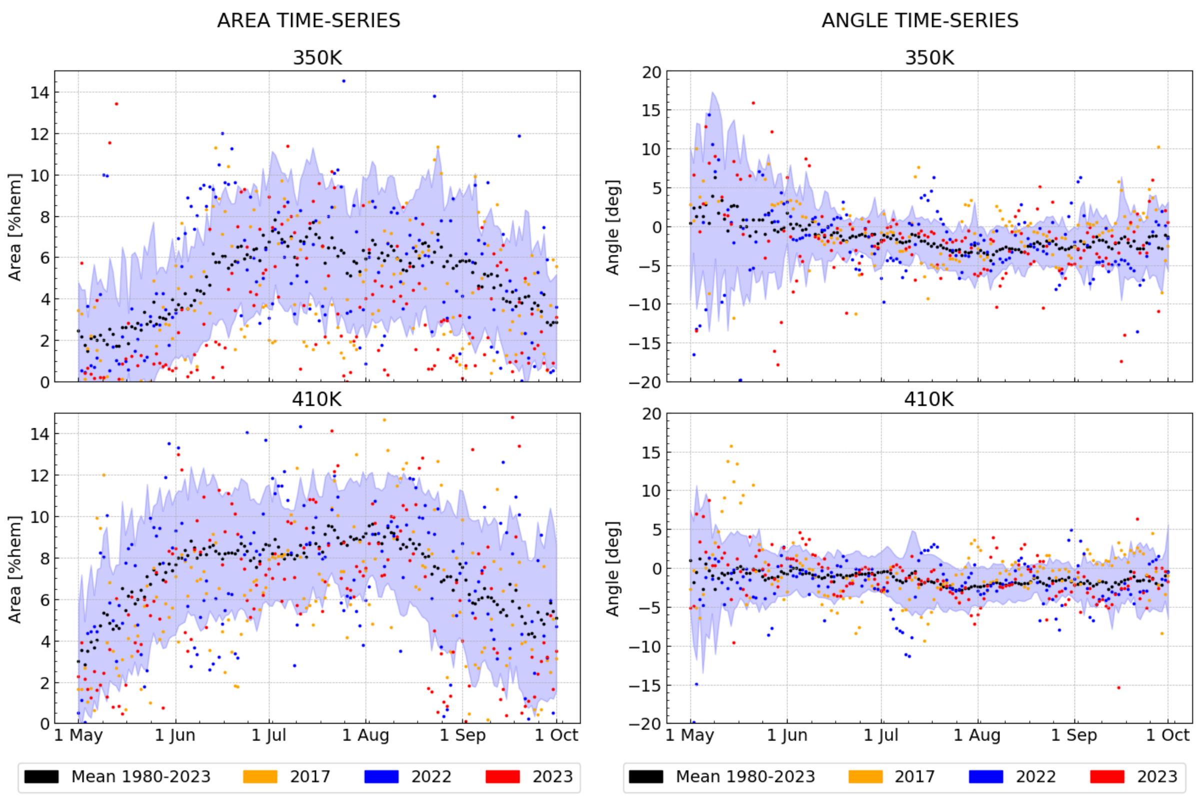

Figure D2. Climatological (1980-2023) time-series (black dots) of the ASMA area (left hand side) and angle (right hand side), and individual years of 2017 (yellow dots), 2022 (blue dots) and 2023 (red dots) at 350 and 410 K. The lavender background denotes one standard deviation of the climatological data.

https://doi.org/10.5194/egusphere-2025-1670
Preprint. Discussion started: 30 April 2025

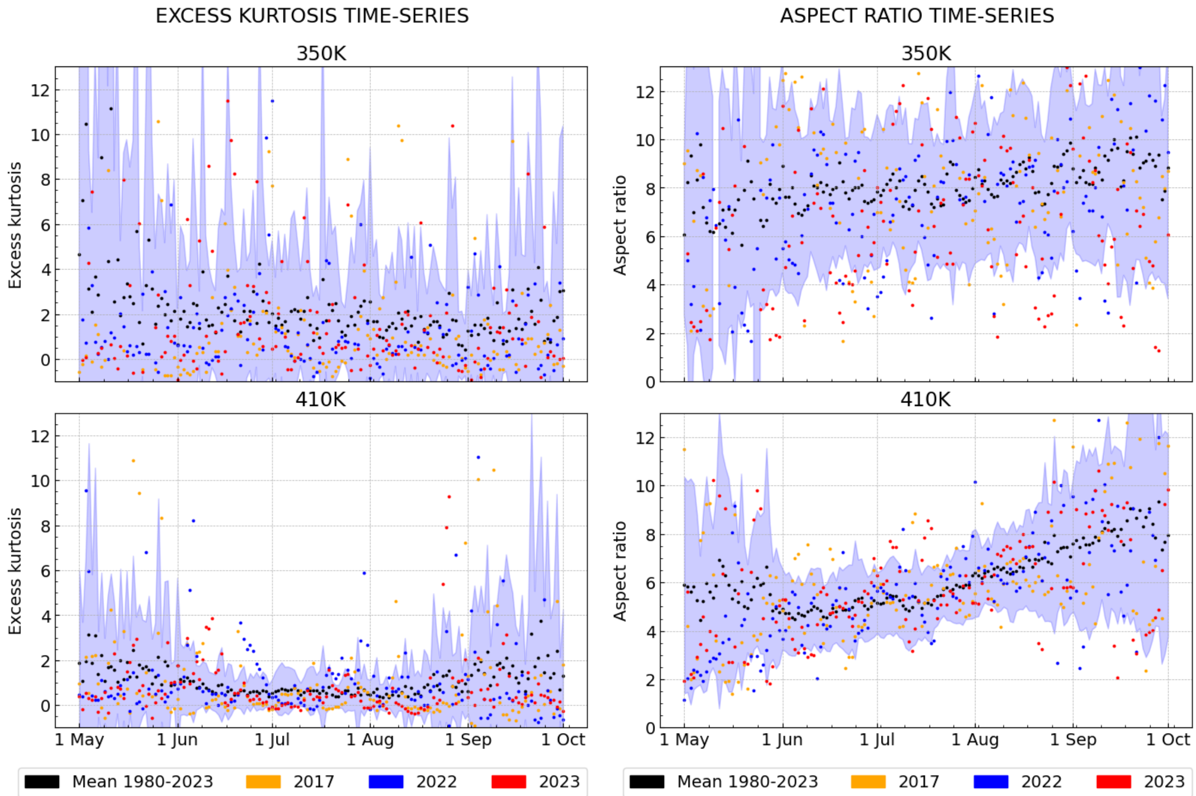

Figure D3. Climatological (1980-2023) time-series (black dots) of the ASMA excess kurtosis (left hand side) and aspect ratio (right hand side), and individual years of 2017 (yellow dots), 2022 (blue dots) and 2023 (red dots) at 350 and 410 K. The lavender background denotes the standard deviation of the climatological data.

Appendix E: Bimodality of the ASMA

https://doi.org/10.5194/egusphere-2025-1670
Preprint. Discussion started: 30 April 2025

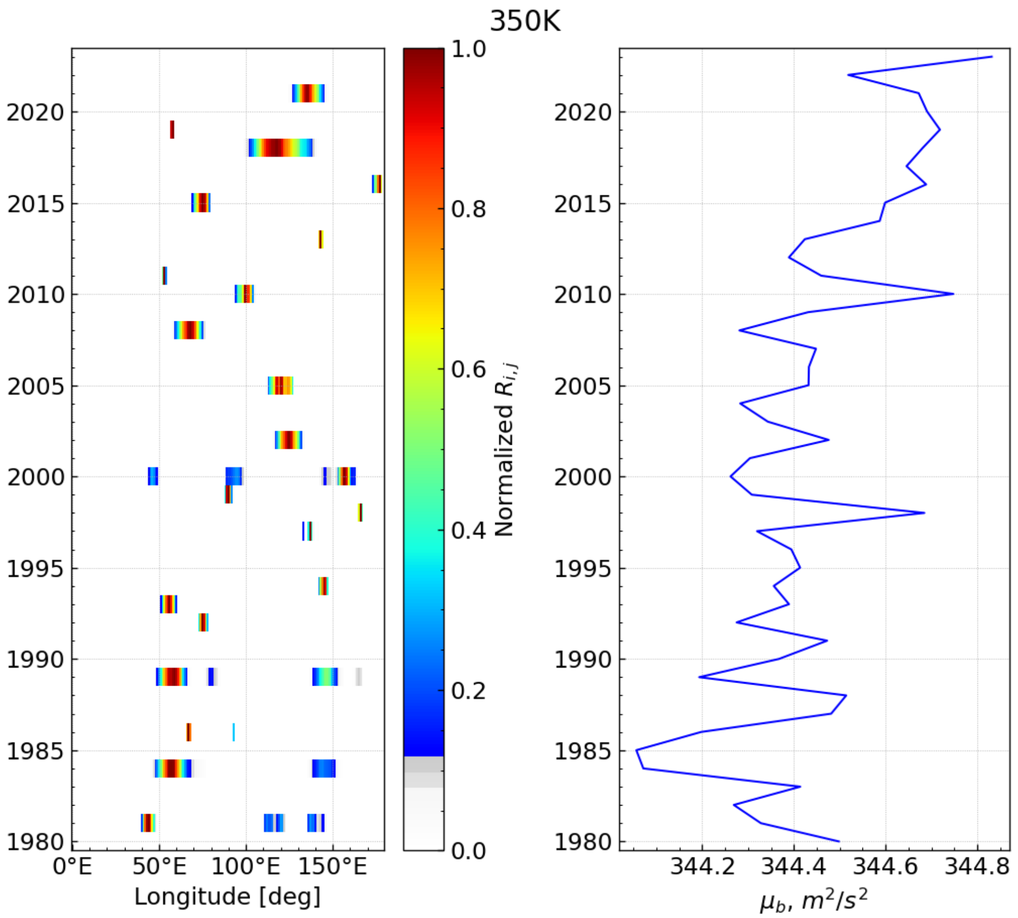

Figure E1. Mean JJA optimized background values (right) and Hovmöller diagram of normalized zonal mean ($15°N - 45°N$) of the residual MSF for 1980-2023 period at 350 K. Reddish colors indicate where the centroid longitudinal position of the ASMA tends to cluster.

https://doi.org/10.5194/egusphere-2025-1670
Preprint. Discussion started: 30 April 2025

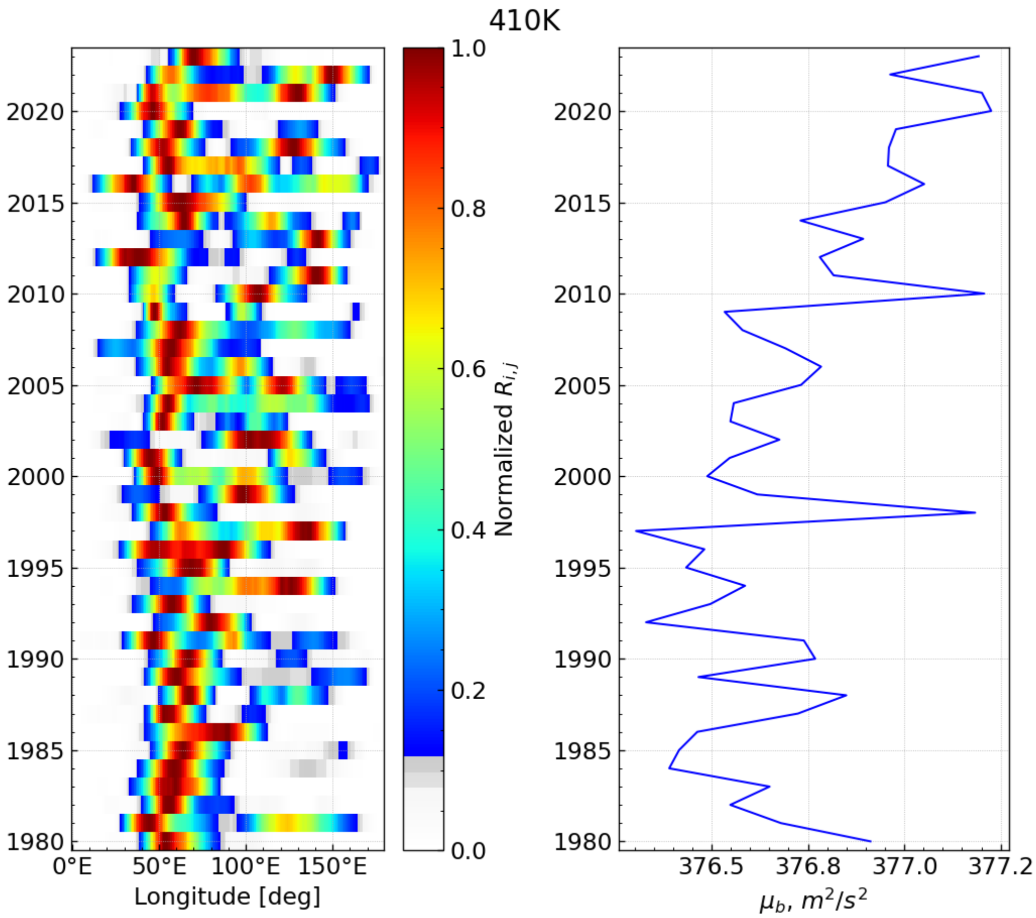

Figure E2. Mean JJA optimized background values (right) and Hovmöller diagram of normalized zonal mean ($15°N - 45°N$) of the residual MSF for 1980-2023 period at 410 K. Reddish colors indicate where the centroid longitudinal position of the ASMA tends to cluster.

Author contributions. The study was conceived by OK, BV and GG. OK designed the method and conducted calculations for this study. BV directed the structure of the paper, analysed the calculated results and supported the study. GG provided advice and guidance for the analysis of the novel method. RM helped to better analyse the bimodality of the ASMA. The results were discussed by all the co-authors. The paper was written by OK with contributions from all the co-authors.

Competing interests. At least one of the (co-)authors is a member of the editorial board of Atmospheric Chemistry and Physics.

https://doi.org/10.5194/egusphere-2025-1670
Preprint. Discussion started: 30 April 2025

Acknowledgements. We thank the European Centre for Medium-Range Weather Forecasts (ECMWF) for providing the ERA5 reanalyses and the Jülich Supercomputing Centre (JSC; Research Centre Jülich, Germany) for the storage resources on the MeteoCloud data archive. The presented work were mainly funded by the German Science Foundation (Deutsche Forschungsgemeinschaft, DFG) as part of the HALO Priority Program SPP 1294 (project VO 1276/7-1). We would like to sincerely thank Michelle Santee (JPL, Pasadena) and Felix Ploeger (FZJ, Germany) for helpful discussions.

References

Adcock, K. E., Fraser, P. J., Hall, B. D., Langenfelds, R. L., Lee, G., Montzka, S. A., Oram, D. E., Röckmann, T., Stroh, F., Sturges, W. T., Vogel, B., and Laube, J. C.: Aircraft-Based Observations of Ozone-Depleting Substances in the Upper Troposphere and Lower Stratosphere in and Above the Asian Summer Monsoon, J. Geophys. Res., 126, e2020JD033 137, https://doi.org/https://doi.org/10.1029/2020JD033137, 2021.

Barret, B., Sauvage, B., Bennouna, Y., and Le Flochmoen, E.: Upper-tropospheric CO and O_3 budget during the Asian summer monsoon, Atmospheric Chemistry and Physics, 16, 9129–9147, https://doi.org/10.5194/acp-16-9129-2016, 2016.

Basha, G., Ratnam, M. V., and Kishore, P.: Asian summer monsoon anticyclone: trends and variability, Atmos. Chem. Phys., pp. 6789–6801, https://doi.org/10.5194/acp-20-6789-2020, 2020.

Chen, G., Du, Y., and Wen, Z.: Seasonal, Interannual, and Interdecadal Variations of the East Asian Summer Monsoon: A Diurnal-Cycle Perspective, Journal of Climate, 34, 4403 – 4421, https://doi.org/10.1175/JCLI-D-20-0882.1, 2021.

Clemens, J., Vogel, B., Hoffmann, L., Griessbach, S., Thomas, N., Fadnavis, S., Müller, R., Peter, T., and Ploeger, F.: A multi-scenario Lagrangian trajectory analysis to identify source regions of the Asian tropopause aerosol layer on the Indian subcontinent in August 2016, Atmos. Chem. Phys., 24, 763–787, https://doi.org/10.5194/acp-24-763-2024, 2024.

Dethof, A., O'Neill, A., Slingo, J. M., and Smit, H. G. J.: A mechanism for moistening the lower stratosphere involving the Asian summer monsoon, Q. J. R. Meteorol. Soc., 556, 1079–1106, 1999.

Fadnavis, S., Sabin, T. P., Roy, C., Rowlinson, M., Rap, A., Vernier, J.-P., and Sioris, C. E.: Elevated aerosol layer over South Asia worsens the Indian drought, Sci. Rep., 9, 10268, https://doi.org/10.1038/s41598-019-46704-9, 2019.

Garny, H. and Randel, W. J.: Dynamic variability of the Asian monsoon anticyclone observed in potential vorticity and correlations with tracer distributions, J. Geophys. Res., 118, 13 421–13 433, https://doi.org/10.1002/2013JD020908, 2013.

Goswami, B. N.: Intraseasonal Variability in the Atmosphere-Ocean Climate System, chap. 2: South Asian monsoon, pp. 21–72, Springer-Verlag Berlin Heidelberg, 2nd edn., editors: W. K. M. Lau and D. E. Waliser, 2012.

Hersbach, H., Bell, B., Berrisford, P., Hirahara, S., Horànyi, A., Muñoz Sabater, J., Nicolas, J., Peubey, C., Radu, R., Schepers, D., Simmons, A., Soci, C., Abdalla, S., Abellan, X., Balsamo, G., Bechtold, P., Biavati, G., Bidlot, J., Bonavita, M., De Chiara, G., Dahlgren, P., Dee, D., Diamantakis, M., Dragani, R., Flemming, J., Forbes, R., Fuentes, M., Geer, A., Haimberger, L., Healy, S., Hogan, R. J., Hólm, E., Janiskovà, M., Keeley, S., Laloyaux, P., Lopez, P., Lupu, C., Radnoti, G., de Rosnay, P., Rozum, I., Vamborg, F., Villaume, S., and Thépaut, J.-N.: The ERA5 global reanalysis, Q. J. R. Meteorol. Soc., 146, 1999–2049, https://doi.org/10.1002/qj.3803, 2020.

Konopka, P., Tao, M., von Hobe, M., Hoffmann, L., Kloss, C., Ravegnani, F., Volk, C. M., Lauther, V., Zahn, A., Hoor, P., and Ploeger, F.: Tropospheric transport and unresolved convection: numerical experiments with CLaMS-2.0/MESSy, Geosci. Model Dev., 15, 7471–7487, https://doi.org/10.5194/gmd-15-7471-2022, 2022.

Kripalani, R. H., Oh, J. H., Kulkarni, A., Sabade, S. S., and Chaudhari, H. S.: South Asian summer monsoon precipitation variability: Coupled climate model simulations and projections under IPCC AR4, Theoretical and Applied Climatology, 90, 133–159, https://doi.org/10.1007/s00704-006-0282-0, 2007.

Kumar, A. H. and Ratnam, M. V.: Variability in the UTLS chemical composition during different modes of the Asian Summer Monsoon Anti-cyclone, Atmospheric Research, 260, 105 700, https://doi.org/https://doi.org/10.1016/j.atmosres.2021.105700, 2021.

Lal, M., Nozawa, T., Emori, S., Harasawa, H., Takahashi, K., Kimoto, M., Abe-Ouchi, A., Nakajima, T., Takemura, T., and Numaguti, A.: Future climate change: Implications for Indian summer monsoon and its variability, Current Science, 81, 1196–1207, 2001.

Lauther, V., Vogel, B., Wintel, J., Rau, A., Hoor, P., Bense, V., Müller, R., and Volk, C. M.: In situ observations of CH_2Cl_2 and $CHCl_3$ show efficient transport pathways for very short-lived species into the lower stratosphere via the Asian and the North American summer monsoon, Atmos. Chem. Phys., 22, 2049–2077, https://doi.org/10.5194/acp-22-2049-2022, 2022.

Manney, G. L., Santee, M. L., Lawrence, Z. D., Wargan, K., and Schwartz, M. J.: A Moments View of Climatology and Variability of the Asian Summer Monsoon Anticyclone, Journal of Climate, 34, 7821 – 7841, https://doi.org/10.1175/JCLI-D-20-0729.1, 2021.

Matthewman, N. J., Esler, J. G., Charlton-Perez, A. J., and Polvani, L. M.: A New Look at Stratospheric Sudden Warmings. Part III: Polar Vortex Evolution and Vertical Structure, Journal of Climate, 22, 1566 – 1585, https://doi.org/10.1175/2008JCLI2365.1, 2009.

Nützel, M., Dameris, M., and Garny, H.: Movement, drivers and bimodality of the South Asian High, Atmos. Chem. Phys., 16, 14 755–14 774, https://doi.org/10.5194/acp-16-14755-2016, 2016.

Pan, L. L., Atlas, E. L., Honomichl, S. B., Smith, W. P., Kinnison, D. E., Solomon, S., Santee, M. L., Saiz-Lopez, A., Laube, J. C., Wang, B., Ueyama, R., Bresch, J. F., Hornbrook, R. S., Apel, E. C., Hills, A. J., Treadaway, V., Smith, K., Schauffler, S., Donnelly, S., Hendershot, R., Lueb, R., Campos, T., Viciani, S., D'Amato, F., Bianchini, G., Barucci, M., Podolske, J. R., Iraci, L. T., Gurganus, C., Bui, P., Dean-Day, J. M., Millán, L., Ryoo, J.-M., Barletta, B., Koo, J.-H., Kim, J., Liang, Q., Randel, W. J., Thornberry, T., and Newman, P. A.: East Asian summer monsoon delivers large abundances of very short-lived organic chlorine substances to the lower stratosphere, Proc. Natl. Acad. Sci., 121, e2318716 121, https://doi.org/10.1073/pnas.2318716121, 2024.

Park, M., Randel, W. J., Emmons, L. K., Bernath, P. F., Walker, K. A., and Boone, C. D.: Chemical isolation in the Asian monsoon anticyclone observed in Atmospheric Chemistry Experiment (ACE-FTS) data, Atmos. Chem. Phys., 8, 757–764, 2008.

Ploeger, F., Günther, G., Konopka, P., Fueglistaler, S., Müller, R., Hoppe, C., Kunz, A., Spang, R., Grooß, J.-U., and Riese, M.: Horizontal water vapor transport in the lower stratosphere from subtropics to high latitudes during boreal summer, J. Geophys. Res., 118, 8111–8127, https://doi.org/10.1002/jgrd.50636, 2013.

Ploeger, F., Gottschling, C., Grießbach, S., Grooß, J.-U., Günther, G., Konopka, P., Müller, R., Riese, M., Stroh, F., Tao, M., Ungermann, J., Vogel, B., and von Hobe, M.: A potential vorticity-based determination of the transport barrier in the Asian summer monsoon anticyclone, Atmos. Chem. Phys., 15, 13 145–13 159, https://doi.org/10.5194/acp-15-13145-2015, 2015.

Ploeger, F., Konopka, P., Walker, K., and Riese, M.: Quantifying pollution transport from the Asian monsoon anticyclone into the lower stratosphere, Atmos. Chem. Phys., 17, 7055–7066, https://doi.org/10.5194/acp-17-7055-2017, 2017.

Ploeger, F., Diallo, M., Charlesworth, E., Konopka, P., Legras, B., Laube, J. C., Grooß, J.-U., Günther, G., Engel, A., and Riese, M.: The stratospheric Brewer–Dobson circulation inferred from age of air in the ERA5 reanalysis, Atmos. Chem. Phys., 21, 8393–8412, https://doi.org/10.5194/acp-21-8393-2021, 2021.

Popovic, J. M. and Plumb, R. A.: Eddy Shedding from the Upper-Tropospheric Asian Monsoon Anticyclone, J. Atmos. Sci., 58, 93–104, 2001.

Randel, W. J. and Park, M.: Deep convective influence on the Asian summer monsoon anticyclone and associated tracer variability observed with Atmospheric Infrared Sounder (AIRS), J. Geophys. Res., 111, D12314, https://doi.org/10.1029/2005JD006490, 2006.

Riese, M., Hoor, P., Rolf, C., Kunkel, D., Vogel, B., Köllner, F., Pöhlker, M., Ploeger, F., Ungermann, J., Woiwode, W., Johansson, S., Bauer, R., Barmpounis, K., Borrmann, S., Brauner, P., Clemens, J., Dragoneas, A., Ekinci, F., Emig, N., Engel, A., Eppers, O., Fadnavis, S., Friedl-Vallon, F., Geldenhuys, M., Günther, G., Grooß, J.-U., Hegglin, M. I., Hoepfner, M., Jesswein, M., Joppe, P., Kaumanns, J., Kachula, O., Keber, T., Kretschmer, E., Lachnitt, H.-C., Lauther, V., Lloyd, P. E., Molleker, S., Müller, R., Neubert, T., Ort, L., Pöschl, U., Pöhlker, C., Rapp, M., Retzlaff, M., Rhode, S., Schneider, J., Schuck, T., Sinnhuber, B.-M., Spelten, N., Strobel, J., Tomsche, L., Turhal, K., van Luijt, R., Versick, S., Voigt, C., Volk, M., von Hobe, M., Weyland, F., Zahn, A., Ziereis, H., and Zlotos, L.: Long-range transport of polluted Asian summer monsoon air to high latitudes during the PHILEAS campaign in the boreal summer 2023, Bull. Am. Meteorol. Soc., in review, BAMS-D-24-0232, 2025.

Santee, M. L., Manney, G. L., Livesey, N. J., Schwartz, M. J., Neu, J. L., and Read, W. G.: A comprehensive overview of the climatological composition of the Asian summer monsoon anticyclone based on 10 years of Aura Microwave Limb Sounder measurements, J. Geophys. Res., 122, 5491–5514, https://doi.org/10.1002/2016JD026408, 2017.

Singer, C. E., Clouser, B. W., Khaykin, S. M., Krämer, M., Cairo, F., Peter, T., Lykov, A., Rolf, C., Spelten, N., Afchine, A., Brunamonti, S., and Moyer, E. J.: Intercomparison of upper tropospheric and lower stratospheric water vapor measurements over the Asian Summer Monsoon during the StratoClim campaign, Atmospheric Measurement Techniques, 15, 4767–4783, https://doi.org/10.5194/amt-15-4767-2022, 2022.

Stroh, F. and StratoClim-Team: First detailed airborne and balloon measurements of microphysical, dynamical, and chemical processes in the Asian Summer Monsoon Anticyclone: overview and selected results of the 2016/2017 StratoClim field campaigns, Atmos. Chem. Phys., to be submitted, 2025.

Turner, A. G. and Annamalai, H.: Climate change and the South Asian summer monsoon, Nature Climate Change, 2, 587–595, https://doi.org/10.1038/nclimate1495, 2012.

Ungermann, J., Ern, M., Kaufmann, M., Müller, R., Spang, R., Ploeger, F., Vogel, B., and Riese, M.: Observations of PAN and its confinement in the Asian Summer Monsoon Anticyclone in high spatial resolution, Atmos. Chem. Phys., 16, 8389–8403, https://doi.org/10.5194/acp-16-8389-2016, 2016.

Vogel, B., Günther, G., Müller, R., Grooß, J.-U., and Riese, M.: Impact of different Asian source regions on the composition of the Asian monsoon anticyclone and of the extratropical lowermost stratosphere, Atmos. Chem. Phys., 15, 13 699–13 716, https://doi.org/10.5194/acp-15-13699-2015, 2015.

Vogel, B., Günther, G., Müller, R., Grooß, J.-U., Afchine, A., Bozem, H., Hoor, P., Krämer, M., Müller, S., Riese, M., Rolf, C., Spelten, N., Stiller, G. P., Ungermann, J., and Zahn, A.: Long-range transport pathways of tropospheric source gases originating in Asia into the northern lower stratosphere during the Asian monsoon season 2012, Atmos. Chem. Phys., 16, 15 301–15 325, https://doi.org/10.5194/acp-16-15301-2016, 2016.

Vogel, B., Volk, C. M., Wintel, J., Lauther, V., Müller, R., Patra, P. K., Riese, M., Terao, Y., and Stroh, F.: Reconstructing high-resolution in-situ vertical carbon dioxide profiles in the sparsely monitored Asian monsoon region, Commun Earth Environ, 4, https://doi.org/10.1038/s43247-023-00725-5, 2023.

Vogel, B., Volk, C. M., Wintel, J., Lauther, V., Clemens, J., Grooß, J.-U., Günther, G., Hoffmann, L., Laube, J. C., Müller, R., Ploeger, F., and Stroh, F.: Evaluation of vertical transport in ERA5 and ERA-Interim reanalysis using high-altitude aircraft measurements in the Asian summer monsoon 2017, Atmos. Chem. Phys., 24, 317–343, https://doi.org/10.5194/acp-24-317-2024, 2024.

Wang, X., Randel, W., Pan, L., Wu, Y., and Zhang, P.: Transient Behavior of the Asian Summer Monsoon Anticyclone Associated With Eastward Eddy Shedding, Journal of Geophysical Research: Atmospheres, 127, e2021JD036 090, https://doi.org/https://doi.org/10.1029/2021JD036090, e2021JD036090 2021JD036090, 2022.

Yan, X., Konopka, P., Ploeger, F., Podglajen, A., Wright, J. S., Müller, R., and Riese, M.: The efficiency of transport into the stratosphere via the Asian and North American summer monsoon circulations, Atmos. Chem. Phys., 19, 15 629–15 649, https://doi.org/10.5194/acp-19-15629-2019, 2019.

Yu, P., Rosenlof, K. H., Liu, S., Telg, H., Thornberry, T. D., Rollins, A. W., Portmann, R. W., Bai, Z., Ray, E. A., Duan, Y., Pan, L. L., Toon, O. B., Bian, J., and Gao, R.-S.: Efficient transport of tropospheric aerosol into the stratosphere via the Asian summer monsoon anticyclone, Proc. Natl. Acad. Sci., 114, 6972–6977, https://doi.org/10.1073/pnas.1701170114, 2017.

Zarrin, A., Ghaemi, H., Azadi, M., and Farajzadeh, M.: The spatial pattern of summertime subtropical anticyclones over Asia and Africa: A climatological review, International Journal of Climatology, 30, 159–173, https://doi.org/https://doi.org/10.1002/joc.1879, 2010.

Zhang, Q., Wu, G., and Qian, Y.: The Bimodality of the 100 hPa South Asia High and its Relationship to the Climate Anomaly over East Asia in Summer, J. Meteorol. Soc. Jpn., 80, 733–744, 2002.